TEL AVIV UNIVERSITY

The Iby and Aladar Fleischman Faculty of Engineering

The Zandman-Slaner School of Graduate Studies

Simultaneous Axial Multifocal Imaging using Frequency Multiplexed Focusing

A thesis submitted toward the degree of

Master of Science in Biomedical Engineering

by

Raphael Abiteboul

This research was carried out in the Department of Biomedical Engineering

Under the supervision of Dr. Tali Ilovitsh

January 23

TEL AVIV UNIVERSITY

The Iby and Aladar Fleischman Faculty of Engineering

The Zandman-Slaner School of Graduate Studies

Simultaneous Axial Multifocal Imaging using Frequency Multiplexed Focusing

A thesis submitted toward the degree of

Master of Science in Biomedical Engineering

by

Raphael Abiteboul

This research was carried out in the Department of Biomedical Engineering

Under the supervision of Dr. Tali Ilovitsh

January 23

Acknowledgments

I would like to sincerely thank my supervisor, Dr. Tali Ilovitsh for her permanent support, her insightful guidance and her confidence during this research. She knew all along the way to give the exact dose between guidance and independence and I'm very grateful for that.

I would also like to thank my parents, for their support and for always encouraging me to pursue my desires. This work would not have been possible without their support.

Finally and most of all, I would like to thank my wife, Deborah, and dedicate this thesis to her for believing in me all the way, supporting me in the challenging periods and pushing me to succeed. Thank you for your love, your motivation, and your endless encouragement.

Abstract

Ultrasound imaging is a widely used medical diagnostics technique enabling real-time, deep penetrating, cost-effective and noninvasive anatomical imaging. Two-way focusing, focusing the signal both on transmit and on receive, yields one of the highest quality ultrasound images. The advantages of the method are its enhanced lateral resolution, signal to noise ratio and penetration depth compared to other ultrasound imaging methods.

One of the limitations of two-way focusing stems from the fact that it only utilizes a single steerable focal spot on transmit that is swept across the field of view. Therefore, in practice, the advantages of two way focusing are confined to the focal region; i.e., the depth of focus (DOF). Successive focusing is the standard method to increase the depth of field of two way focusing by transmitting two steered focused beams to different depths successively. This method generates multiple focal zones, at the expense of a reduced framerate that is proportional to the number of generated foci. Recently, a method for simultaneous axial multifoci imaging (SAMI), based on temporal superposition of axial multifoci waveforms in a single transmission was developed to enhance the depth of field without compromising the frame rate. However, since all the waveforms are transmitted at a constant center frequency, there is a tradeoff between attenuation and lateral resolution when choosing a constant frequency for all the axial depths.

The purpose of this work was to develop an optimized SAMI method by adding frequency dependence to each axial multifocus. By gradually increasing the frequency as a function of the focal depth, this method makes it possible to compensate for the gradually increasing F-number in order to achieve constant lateral resolution across the entire field of view. Alternatively, by gradually decreasing the axial multifoci frequencies as a function of depth, enhanced penetration depth and contrast are obtained.

This method, termed frequency multiplexed SAMI (FM-SAMI) is described analytically and validated by hydrophone scans, and resolution and contrast experiments performed on resolution targets, tissue-mimicking phantoms and ex-vivo biological samples. This is the first real-time implementation of a frequency multiplexing approach for axial multifoci imaging that facilitates high quality imaging at an increased framerate.

Contents

Abbreviations and symbols

BF …….…..…… Beamforming	MPa …… Mega Pascale
B-mode ..…….……..... Brightness mode	PNP ……..... Peak negative pressure
BW …….…..... Bandwidth	PSF ……. Point spread function
CR …..……...……... Contrast ratio	PW……...…….. Plane-wave
DAS ..…… Delay and sum	PZT ……..... Lead-zirconate-titanate
DOF …….. Depth of focus	RF ……..... Radiofrequency
FDA ..…… Food and Drug Administration	SAMI ….. Simultaneous Axial Multifocal Imaging
FOV …….....…..... Field of view	FM-SAMI ... frequency multiplexed SAMI
FWHM ……..…..….. Full-width-half-max	TIS ……..…..…. Thermal index
Ispta ……. Intensity spatial peak temporal Average	US ……...……..……..... Ultrasound
MI …….……....…... Mechanical index	Vpp …….. Peak-to-peak voltage
MHz ……..... Mega Hertz	
T_R ……..... Pulse repetition interval	τ [sec] ……..……. Time delay
$f_R \left[\frac{1}{sec}\right]$ …….. Pulse repetition interval	$t_{line}[sec]$ ... Time to obtain one scan line
$c \left[\frac{m}{sec^2}\right]$ ….……..… Speed of sound	N_{line} …….. Number of scan-lines
z $[mm]$……..... Depth	$T_{frame}[sec]$ … Time to obtain one frame
p [MPa] ….……..…….…… Pressure	FR $[Hz]$……..……..... Frame rate
$\rho \left[\frac{kg}{m^3}\right]$ ...….……..…… Density	W_i .. Apodization coefficient of element i
κ $[Pa^{-1}]$ ...……..……Compressibility	n ……..……..…… Focus index
$\omega \left[\frac{\text{rad}}{sec}\right]$ ……..... Angular frequency	λ ……..……..…….. Wavelength
k ……..……...….. Wave number	f ……...……..……..... Frequency
Z $[Rayl]$ ……..... Acoustic impedance	D ……....……....….. Aperture width
$I \left[\frac{W}{m^2}\right]$..…….... Intensity	$F\#$ ..…….…..... F-number
θ [°] …… Angle	$\alpha_{dB}[dB]$ ……..... Attenuation coefficient
x …….. Lateral coordinate	α $[D]$ ….…..... Overlapping aperture area
y …….. Elevation coordinate	N …….. Number of transmitted cycles
z ..…….... Axial coordinate	μ_i ..... Mean pixel value inside the object
	μ_o ... Mean pixel value in the background
	$W_{01}[mW]$ …….. Power

List of figures

List of tables

List of Publications

Journal paper:

- **Raphael Abiteboul** and **Tali Ilovitsh**, “Optimized Simultaneous Axial Multifocal Imaging via Frequency Multiplexed focusing", in IEEE Transactions on Ultrasonics, Ferroelectrics, and Frequency Control, vol. 69, no. 10, 2930-2942, 2022.

Conference presentations:

- **Raphael Abiteboul**, “Optimized Simultaneous Axial Multifocal Imaging via Frequency Multiplexed focusing." Seminar of the Biomedical Engineering Department, Tel Aviv University, Israel, May 2022. (Oral presentation).

1 Introduction

Ultrasound imaging is a widely used medical diagnostics technique enabling real-time, deep penetrating, cost-effective and noninvasive anatomical imaging [1], [2]. In addition to the wide variety of human medicine applications that diagnostic US has been used for, diagnostic US extensively contributed to the development of the veterinary medicine too. Nowadays, the main medical applications based on US imaging are female breast, cardiac, gynecologic, radiology (internal organs of the abdomen), obstetrics (fetuses in vivo), vascular system, etc [3]. The many advantages US has on its competing imaging methods yielded a great interest among many research groups. For example, the fact that US doesn't involve the use of ionizing radiation makes it – if used properly - safer than CT and X-ray imaging and actually enables unlimited imaging time (under the required safety limits). Moreover, its affordability makes it much more accessible than other expensive imaging methods such as MRI, CT and PET [3].

Thanks to the many benefits obtained by using US system for diagnostic technical advances in the field of diagnostic US are constantly being made, while existing methods are constantly optimized, and even novel modalities are invented. Most of the newly software-based US methods developed in the last decade, especially real-time imaging, were enabled by the constant improvement of hardware and software abilities [4]. Improving US performance would enable to improve the accuracy of diagnosis, to improve monitoring (e.g., cancerous tissues), and even to obtain a better assistance of US guided procedures and therefore it is of great interest.

Two-way focusing, typically applied in B-mode imaging, yields one of the highest quality ultrasound images by steering a focused beam across the field of view [5]. On transmit, the focal beam is generated by transmitting a parabolic waveform with the transducer array elements, such that the beam creates a constructive interference at a specific depth [6]. Beamforming is used to

focus the beam on receive, yielding a two-way focused image [7]. The advantages of the method, compared for example to one-way focusing where a planar wave illuminates the entire field of view and is focused only on reception, are its enhanced lateral resolution, signal to noise ratio and penetration depth [8]–[11].

One of the limitations of two-way focusing stems from the fact that it only utilizes a single steerable focal spot on transmit that is swept across the field of view. Therefore, in practice, the advantages of two way focusing are confined to the focal region; i.e., the depth of focus (DOF). Successive focusing is the standard method to increase the depth of field of two way focusing by transmitting two way steered focused beams to different depths successively. This method generates multiple focal zones, at the expense of a reduced framerate that is proportional to the number of generated foci [12], [13]. Recently, a method for simultaneous axial multifoci imaging (SAMI), based on temporal superposition of axial multifoci waveforms in a single transmission was developed. It uses temporal superpositioning of multiple waveforms, where each wavefront is focused to a different depth. By transmitting the combined waveform, axial multifoci imaging is achieved using a single acoustical transmit. Thus, an enhanced framerate is obtained compared to successive focusing, while maintaining high lateral resolution and depth of field [1]. Although SAMI is efficient in generating axial multifoci, it is limited by the fact that all of the waveforms are transmitted at a constant frequency. Here, a frequency multiplexed SAMI (FM-SAMI) method is presented. The method makes it possible to transmit each superpositioned waveform at a different frequency so that the generated axial multifoci are frequency dependent. By adapting the frequency of each focus, high lateral resolution at shallow depths along with enhanced penetration for the deeper depths can be obtained. In addition, uniform lateral resolution as a function of depth also becomes feasible. The FM-SAMI method is implemented

in real-time using a programmable ultrasound system that can dynamically modify the transmitted pulses for each transducer element separately using a built-in arbitrary waveform generator [14], [15].

The concept of focal depth dependent frequency has been addressed in several methods. However, these methods compromise frame rate, axial resolution, or require post processing on receive. One of these methods is frequency-dependent successive focusing, where the frequency of each transmitted focus is adjusted as a function of depth [16]. Similar to standard successive focusing, it reduces the frame rate in proportion to the number of foci. Another method uses a custom system design. The system is composed of several multi-channel transmitters, each with a different frequency [17]. This setup is mechanically complex, as it utilizes multiple co-aligned transducers, and requires adaptation per patient and target location. Another category of methods includes the transmission of long pulses and the application of post processing on receive. Examples include the transmission of a chirp-like broadband multifrequency pulse, with high frequencies that focus to a shallow depth and low frequencies that focus to a deeper depth. On receive, a time varying bandpass filter whose center frequency decreases with depth is applied [18]–[20]. Finally, the use of orthogonal frequency division multiplexing in parallel transmit beamforming can be used to extend the DOF; however, this approach uses orthogonal codes that degrade resolution, in combination with additional post processing on receive [21]–[23].

The FM-SAMI method uses single cycle excitation, and hence maximizes axial resolution. It is implemented in real time and employs standard receive beamforming that is identical to two-way focusing without additional post processing. It makes it possible to achieve axial multifoci imaging at an enhanced framerate, while adapting each focus' frequency to yield an optimized tradeoff between spatial resolution and penetration depth.

This thesis describes the different stages in the optimization of the novel imaging method termed FM-SAMI, from theoretical simulations to validation of the method through US experiments using hydrophone scans, resolution and contrast targets, and ex-vivo biological samples. First, the main objectives of this research are presented in chapter 2. Then, chapter 3 introduces a general background of US imaging principles, including a presentation of the standard processes used in the transmit and the receive stages of two-way focusing imaging, the improved methods available in the clinics and the motivation on which the development of the proposed method is based. Furthermore, at the end of the 3rd chapter the concept of the proposed method is presented. Chapter 4 presents the methods and materials which were used for this work, including the design of the transmission signal and a description of the setups used for the different experiments performed in order to validate the proposed method. Following, the numerical simulations results are presented in chapter 5 as well as the experimental results including the evaluation of the FM-SAMI method using hydrophone scans, resolution and contrast targets, and ex-vivo biological samples. Finally, chapter 6 discusses the implications and draws conclusions, together with the limitations and further possible optimizations of the proposed method.

2 Research objectives

This work aims to add frequency dependence to each transmitted focus in multifoci imaging and enhance the performance of the current SAMI method. By generating frequency-dependent axial multifoci as a function of depth, an optimized tradeoff between spatial resolution and penetration depth could be achieved. The research had two main objectives that are not feasible using conventional SAMI:

- Enable a more uniform lateral resolution across the field of view by transmitting the lowest frequency to the shallowest focus, and gradually increasing the frequency as a function of depth (i.e. “FM-SAMI Increasing”)
- Optimize the tradeoff between lateral resolution and depth penetration by gradually decreasing the frequency as a function of axial multifoci. This approach will enhance penetration depth for the lower frequencies, and maintain high resolution for shallow distances (i.e. “FM-SAMI Decreasing”).

3 Theoretical Background

For a better understanding of the thesis and the proposed US imaging method, the main principles of US imaging in general and then of the conventional method used nowadays in order to increase the depth of field, should be presented. Moreover, standard SAMI using constant frequency, which is the imaging method this study aims to optimized, should also be introduced. Therefore, this chapter presents the most important aspects of US imaging, including the basic physical phenomenon, commonly used transducers, imaging modalities, and evaluation metrics, based on two US books [24], [25].

3.1 Ultrasound imaging principles

US is an imaging method that uses sound waves with frequencies exceeding the upper audible limit of human hearing. Because ultrasound is a wave, it transmits energy just like electromagnetic wave or radiation. Unlike an electromagnetic wave, sound requires a medium to travel through it and thus can't propagate in vacuum. This implies that there is a strong relation between the properties of the medium (e.g., structure, elasticity, density, etc.) and the corresponding acoustic properties of the acoustic waves (e.g., speed of propagation, attenuation,

possible wave types, etc.) passing through it. These high frequency acoustic waves, also termed pressure waves, propagate in the medium thanks to its expansion and compression while the velocity of propagation depends on the properties of the medium. The potential of ultrasound as an imaging modality was discovered when during World War II several research groups, inspired by sonar and radar technology, started exploring the diagnostic capabilities of ultrasound. The primary form of ultrasonic imaging to date has been that of a pulse-echo technique, whose principle is very similar to sonar and radar. In essence, following the transmission of acoustic signal, echoes from the medium being insonated are detected and used to form an image [24]. Although pulse-echo ultrasound had been used for the diagnosis of a variety of medical problems, it didn't become a widely accepted diagnostic tool until the introduction of grayscale images, termed B-mode images.

US imaging, based on piezoelectric transducers that convert electric signals to acoustic signals (and vice versa), provides a noninvasive technique for imaging human anatomy. Note that the same transducer is used for both transmission and reception of the ultrasound waves in the medium. Standard ultrasound imaging methods consist of transmitting short acoustic pulses at specific center frequency while focusing them at a desired depth, determined according to the region of interest [26]. Due to the inhomogeneity of the medium caused by the variety of tissues and organs the human body is consisted of, the acoustic waves are partially reflected and scattered, generating echoes that propagate back toward the transducer with the same frequency spectrum [27]. Then, through the piezoelectric elements of the transducer, these acoustic echoes are converted to electrical signal (raw channel data) that after processing by the system's software yields the grayscale image called B-mode image. In the image generated, the anatomic structure sonicated is quantized into pixels whose brightness corresponds to the strength of the echo

received from the regions covered by them [28]. The position of the received echo in the picture is determined by both the beam direction in the plane and its acoustic transit time. According to that, the frame rate actually depends on the furthest point included in the zone of interest. Given a maximal scanning depth of z_{max} and acoustic velocity of c, the pulse repetition interval, T_R, and the pulse repetition rate, f_R, are calculated as follow [24]:

$$T_R = \frac{2z_{max}}{c}, \quad f_R = \frac{1}{T_R} \tag{1}$$

3.2 Sound propagation in a medium

The source of acoustic wave is a change in stress or pressure of acoustic field within the medium – for example, a clap of hand or an explosion. The propagation of these waves is actually a process of mechanical energy flow, which is embedded in the medium in the form of elastic strains and vibrations of the medium, from one place to another. When a change in the pressure field of the medium occurs, kinetic energy is transferred to its particles, causing them to vibrate. As a result, part of the kinetic energy is transferred to the next adjacent particles, therefore creating a chain reaction and diminishing their motion until they are affected by another disturbance in the pressure field. If the driving force is oscillating back and forth or sinusoidally, the particles respond by oscillating in the same way, creating alternating rarefaction and compression patterns through the medium (Figure 1). In the compression regions, the particle density is the highest, causing high pressure, whereas the rarefaction regions are characterized by low pressure and therefore low particle density too. Moreover, since the displacement of the particles is in the same direction as the direction of wave propagation, this type of wave is part of waves called longitudinal wave [4], [25], [29].

Due to their high-water content, soft tissues have acoustic properties very similar to those of water and therefore acoustic waves propagation through them can be approximated as waves propagation in fluidic material. This simplification enables to assume that the waves propagating in soft tissues, unlike the waves propagating in solids, are mainly longitudinal waves. Another convenient simplification is that acoustic waves behave linearly. In other words, it means that changes in the amplitude of the waves don't affect their shape that remain the same and that the combination of several different waves at the same location form a superposition wave. This superposition principle is at the heart of the designs of almost all ultrasound imaging systems [24].

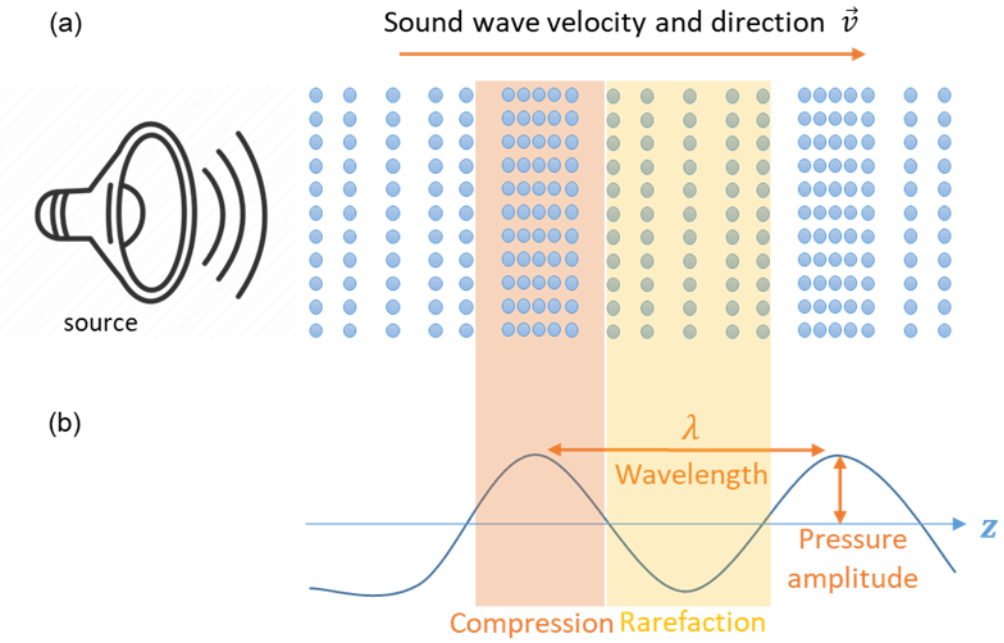

Figure 1. Propagation of longitudinal wave illustration. (a) One dimensional sound wave propagates by compression and rarefaction of particles in the medium. (b) Pressure graph produced by the sound wave in (a), displayed as a transverse wave.

The phenomenon of acoustic wave propagation is commonly described by the wave equation. For simplicity, the second-order differential wave equation will be described for **a homogeneous** medium without attenuation, at a position (x, y, z) in the propagating space and at a time *t* [25]:

$$\nabla^2 p - \frac{1}{c^2}\frac{\partial^2 p(x,y,z,t)}{\partial t^2} = 0, \quad \nabla^2 p = \frac{\partial^2}{\partial x^2}p + \frac{\partial^2}{\partial y^2}p + \frac{\partial^2}{\partial z^2}p\,, \tag{2}$$

where ∇^2 is the Laplacian operator and c is sound velocity in the medium, defined as:

$$c = \frac{1}{\sqrt{\kappa\rho}}, \tag{3}$$

where ρ is the medium density and $\kappa[Pa^{-1}]$ is its compressibility. The average speed of sound for soft tissues is 1540 m/s. Although air is characterized by small density, its compressibility is significantly larger than this of water and therefore the speed of sound in air is much smaller than in water. Given a plane-wave (PW) which propagates in positive x direction only, the wave propagation will be describe as:

$$\frac{\partial^2 p(x,t)}{\partial x^2} - \frac{1}{c^2}\frac{\partial^2 p(x,t)}{\partial t^2} = 0, \tag{4}$$

where $p(x,t)$ is the pressure, which depends on the position *x* and the time *t*. One of the possible general solutions of (4) can be:

$$p(x,t) = p_0 e^{j(\omega t - kx)}\ , \tag{5}$$

where p_0 is the amplitude of the propagating wave, ω is the angular frequency, and $k = \frac{\omega}{c}$ is the wavenumber. Furthermore, it is common to represent the acoustic pressure by its magnitude, i.e., the real part of the expression in (5):

$$p(x,t) = p_0 \cos\left(\omega\left(t - \frac{x}{c}\right)\right). \tag{6}$$

For plane-wave, the sound intensity *I*, which is defined as the power carried by the wave per unit area normal to the direction of propagation, is proportional to the amplitude of pressure oscillations [24]:

$$I = \frac{1}{T}\int_0^T p(t)\cdot v(t)dt \tag{7}$$

The ratio between the generated pressure, *p*, and the particle velocity of the medium, *v*, is a specific acoustic property of the medium, known as the acoustic impedance *Z*. Equivalently, the acoustic impedance can also be described by the product of the medium density and the speed of sound [28]:

$$Z\ [Rayls] = \frac{p(t)}{v(t)} = \rho c, \tag{8}$$

while impedance's units are Rayls and $1[Rayl] = 1\left[\frac{kg}{m^2\cdot sec}\right]$. By extracting particle velocity from (8) and substituting it, together with the pressure from (6), into (7), intensity can be described as:

$$I = \frac{{p_0}^2}{2Z}\left[\frac{W}{m^2}\right] \tag{9}$$

When a PW hits a boundary, separating two mediums with different acoustic properties, the acoustic impedance changes cause the incident wave energy to split while a certain fraction of it is reflected from the interface, and the remainder is refracted. Regarding the reflecting fraction, the angle it forms with the normal of the interface, θ_r, is equal to the angle which the incident wave energy makes with the same normal, θ_i, on its opposite side. Regarding the refracted fraction, it continues to propagate further the following medium with some deviation from the incident wave direction caused due to the differences in the speed of sound of the different

mediums (Figure 2). The angle in which the refracted wave, termed also as the transmitted wave, θ_t, propagates in the following medium, can be calculated using the acoustic Snell's law:

$$\frac{sin\theta_i}{sin\theta_t} = \frac{C_1}{C_2} \tag{10}$$

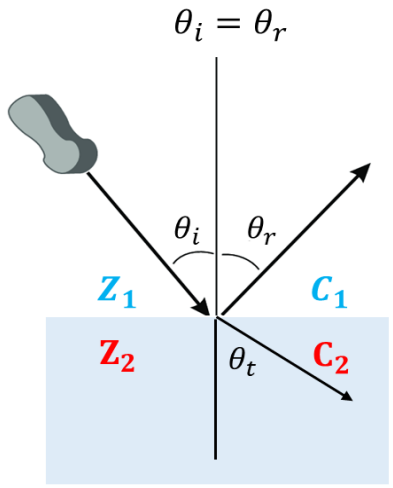

Figure 2. Illustration of reflection and refraction (transmission) of the incident acoustic wave which occurs at the interface between two mediums with different acoustic impedance Z_1, Z_2 and different speed of sound C_1, C_2. θ_i is the incident angle, θ_r is the reflection angle and θ_t is the transmission angle.

When waves propagate in real media, losses, also called "attenuation", are involved. Absorption in the body is a major effect since it limits the detectable penetration of sound waves in the body. These losses are described by an exponential law that attenuate the propagating pressure with distance. That is, for a plane-wave transmitted into a medium whose attenuation coefficient is α, a multiplicative amplitude loss term should be added to the pressure wave representation in (5) so that a more accurate expression of the pressure is obtained, as follow:

$$p(x,t) = p_0 e^{j(\omega t - kx)} \cdot e^{-\alpha x} \tag{11}$$

where x is the distance travelled by the sound wave in the penetration direction and α is as mentioned the attenuation coefficient, dependent on medium viscosity and on wave frequency like it will be elaborate later [24].

3.3 Transducers

The one indispensable part of a diagnostic system is the transducer. Transducers comes in a variety of shapes, sizes, and bandwidths, adapted to the clinical application and the scanning method required. For basic intuition, the simplest transducer consists of a piece of piezoelectric crystal material, such as lead-zirconate-titinate, whose both sides are connected to electrodes. As mentioned earlier, piezoelectric material enables to convert electric signals into acoustic signals (and vice versa). Therefore, by applying a potential gradient across the electrodes, the piezoelectric material resonates at its center-frequency, generating a pressure wave and therefore equivalently, an acoustic signal [30]. This center-frequency is defined by the transducer's bandwidth frequency which mostly ranges from 1 MHz to 15 MHz for diagnosis systems. Thanks to the inverse ability of piezoelectric materials to convert acoustic signals into electric signals, most ultrasound transducers are used as receivers also. If the frequency of the echoes reflected is within the frequency bandwidth of the transducer, it will be detected and transferred to electrical signal [24].

The first transducers were composed of a single piezoelectric element, as described until here. This fact limits their practicality in the clinic since it enables them to generate only geometrical focus which in addition could be generated only at a fixed depth. Therefore, the transducers had to be steered mechanically to focus the entire region of interest. These two restrictions limited dramatically the imaging depth, the resolution, and the real-time imaging performance. In order to overcome this, multi-elements arrays were invented (Figure 3). They consist of multiple small piezoelectric elements that can be excited individually and separately. Moreover, it offers the ability to focus beams electronically, at different depths and angles, by controlling the phased delay excitation of each element and without moving any parts of the transducer. It therefore

enables a higher flexibility to focus the waveforms at a larger range of depths and also to decrease significantly the scanning time required to complete an entire image. In addition, multi-elements arrays enable to control also the apodization of each element separately, that is to apply different weighting coefficients to each element's excitation signal. Nowadays, these kinds of arrays became the standards transducers for US imaging systems in clinics, including generally between 64 to 512 piezoelectric elements [31].

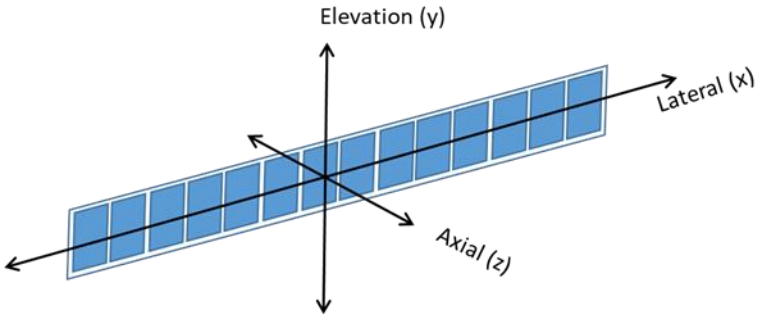

Figure 4. The spatial coordinate system for 1-D ultrasound transducer of multi-elements array. The transmitted ultrasound wave propagates in the axial direction, which is also the normal to the elements' surface.

Focus spots are generated by causing the excitation signals of all the transducer's elements to constructively interfere at a desired location. Electronically, it is implemented by controlling the delay of each excitation, such that different elements transmit their signal at different times while their emission is delayed relatively to the element closest to the focal location. More specifically, the transmission time delay of each element is determined by the difference in the time required from its excitation to reach the focal location compared to the time required for the excitation of the closest element of the transducer to reach this same location (Figure 4). For example, in order to generate a focal spot at a general location (x_f, y_f, z_f) through a multi-element array, the negatively signed delay time, τ, required from the i-th element in order to create a constructive interference at the focal point is defined as [28]:

$$\tau_i(x_f, y_f, z_f) = \frac{1}{c}\left(\sqrt{(x_c - x_f)^2 + (y_c - y_f)^2 + (z_c - z_f)^2}\right. \\ \left. - \sqrt{(x_i - x_f)^2 + (y_i - y_f)^2 + (z_i - z_f)^2}\right) \tag{12}$$

where (x_c, y_c, z_c) are the coordinate of the transducer's element closest to the focal point and (x_i, y_i, z_i) is the coordinate of the piezo-electric element i for which the time delay is calculated. The waveforms obtained for standard focusing are generally parabolic while the more concave the parabola is, the closer the focus region is from the transducer aperture.

As mentioned before, depending on the clinical application and the scanning method required, US transducers appear in a wide variety of shapes, sizes, and bandwidths. The three most conventional configurations are linear, phased, and convex arrays. Figure 5 presents these three common types of arrays and the electronic steering implementation of the transmitted beams for each case [32].

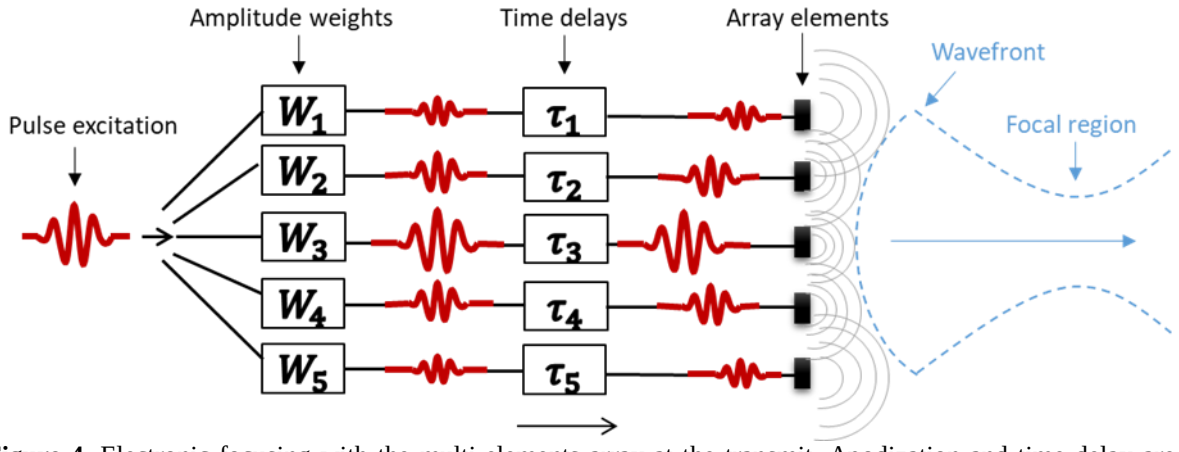

Figure 4. Electronic focusing with the multi-elements array at the transmit. Apodization and time delay are applied to each element's excitation pulse.

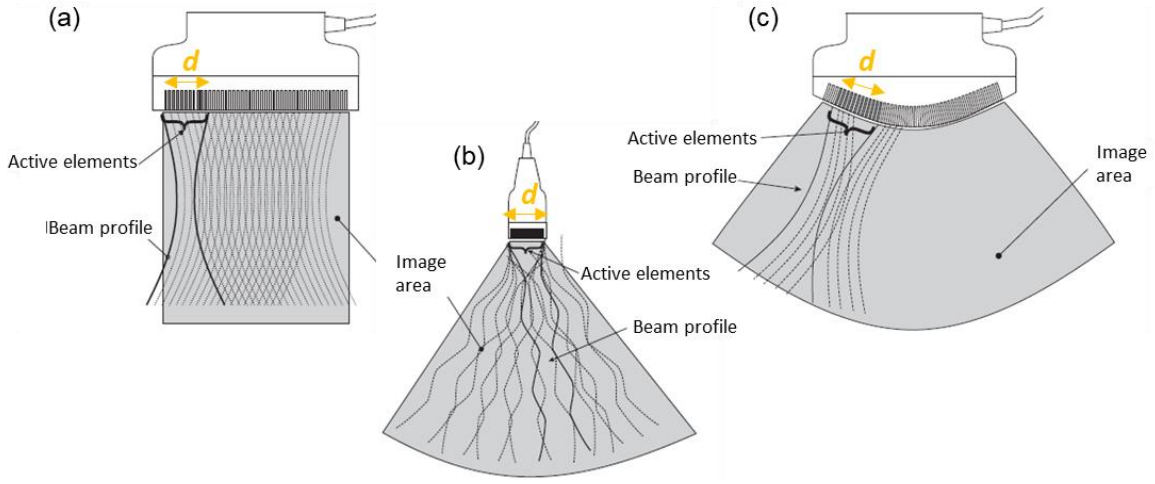

Figure 5. Illustration of three major multi-elements array transducer types: (a) Linear array, (b) Phased array, (c) Convex array, and their corresponding steering implementation. *d* represents aperture width determined by the number of active elements.

3.4 Two-way focusing

B-mode imaging is a real-time gray scale imaging method that depicts the reflectivity of structures within the field of view. Due to in-homogeneities of the speed of sound and the density within each voxel, the transmitted sound waves scatter. According to the strength of the echo, the brightness of the pixel in the picture is determined [33]. From the variety of B-mode imaging methods, two-way focusing yields one of the highest quality ultrasound images by steering a focused beam across the field of view (FOV). A pulsed wave is first directed along a straight-line direction and focused at a specific depth in this direction. Once the echoes are received, the beam is moved and transmitted to a new sampling direction. A single image is formed by sweeping the beams along multiple scanning directions throughout the FOV while typical two-way focusing images are generally composed of 64 to 512 scan lines.

Two-way focusing imaging is commonly implemented through the three main array transducer types presented earlier. Using linear array (Figure 5. (a)), each scan-line is acquired by transmitting with a different part of activated elements of the array, termed as sub-aperture. These

sub-apertures contain typically 5-20 elements and are shifted over a region of interest in the body. I.e., the active elements are moved stepwise from one extremity of the aperture to the other while at each step a new focused beam is emitted and its echoes are received. This process is repeated until all the transducer's elements have contributed to the transmit process. Through array of this kind, the FOV scanned is rectangular and therefore the image obtained is rectangular too. This kind of transducers are characterized by relatively high transmission frequencies, compared to phased array transducers, leading to limited depth penetration, and therefore are usually used for shallow objects imaging. For phased array transducers (Figure 5. (b)), the active aperture is standardly centered in the middle of the array while the aperture may vary in the number of elements excited at any given time. With this kind of transducers, the scanning of acoustic lines is accomplished sequentially through electronic angular steering, i.e. each scan-line is steered by a small incremental angle from the previous one, until a sector is covered, yielding therefore an image with a sector shape too. Such arrays are typically composed of smaller elements than linear and curved arrays (in the order of half the wavelength) and since the transducer's number of elements is generally similar between phased, linear and curved arrays, the aperture size is often smaller for phased arrays compared to linear and curved arrays. Thanks to their relatively small physical size, arrays of this kind are characterized by small contact surface area with the body while enabling to image a large region in the body. Common application of such arrays is for example cardiac imaging since the aperture has to be small enough in order to fit the intercostal spaces between the ribs and reach the heart properly [26]. For convex array transducers (Figure 5. (c)), the implementation of line sequencing is similar to those of linear array, i.e. sub-apertures are used and the active elements are stepwise shifted along the aperture, except that each sub-aperture is composed of more active elements. They combine the advantage of yielding a larger

angular image with ease of linear array scanning, i.e. producing focal delay at straight direction without requiring electronic steering for each line [24].

The combination of all the scan-lines acquired forms a single frame while the whole data acquisition process described is continually repeated in order to update the FOV and even to depict motion in few applications. Therefore, the frame rate of two-way focusing imaging is actually limited by the number of scan-lines, required for good spatial resolution, and by the time of acquisition of a single scan line, t_{line}, that is determined by the transit time of the ultrasound pulse until it reaches the depth of interest and returns as an echo to the transducer. That is, given an image composed of N_{line} scan-lines, acquired in a tissue in which the speed of sound is c and up to a scan depth of z_{max}, the frame rate f_R is calculated as described below:

$$f_R = \frac{1}{T_{frame}} = \frac{1}{t_{line} \cdot N_{line}} = \frac{1}{\frac{2 \cdot z_{max}}{c} \cdot N_{line}} \tag{13}$$

On one side, reducing the number of scan lines enables to increase the frame rate. On the other side, it is likely to decrease scan line density such that the separations between adjacent scan lines became larger than the beamwidth, yielding a decreased lateral resolution. I.e., image resolution and frame rate compete with each other.

Although the method developed in this work focuses mainly on improving the transmit stage of the imaging process, the standard process applied on the receive signal shall be discussed nevertheless such that the integrality of the imaging process would be presented. Thus, after presenting the main concepts concerning the transmit and the scanning stages, the image formation from the received echoes will be elaborated here. At the end of the beam formation and the scanning process, the echo-responses detected from the different scanning directions by the transducer's elements yield signal termed as raw channel data. Then, these raw channel data are passed into the main stage in the image reconstruction process, termed as beamforming (BF).

This stage has two main roles. First, it improves the image quality, and more specifically the lateral resolution, the contrast and the signal to noise ratio. Second, it focuses the receive beam dynamically such that echoes from all depths are always in focus. Because the change of focal length in reception can be done electronically in real-time, the process does not reduce imaging frame rate and therefore it is widely used in commercial diagnostic imaging equipment. The BF stage consists of integrating the receive signals reflected to the transducer with appropriate weighting (apodization) and time delays (for focusing). In other words, it enables to deliberately prioritize echoes that are reflected from some known positions rather than the signal reflected from other positions that as a result is artificially attenuated and therefore this stage is often considered as spatial filtering. This concept, illustrated in Figure 6 and further detailed in Figure 7, contribute to the obtainment of a single RF signal and is also known as delay and sum (DAS) process [26]. It should be noted that the process of designing the transmitted beam, enabled via multi-array transducers, is called beamforming too.

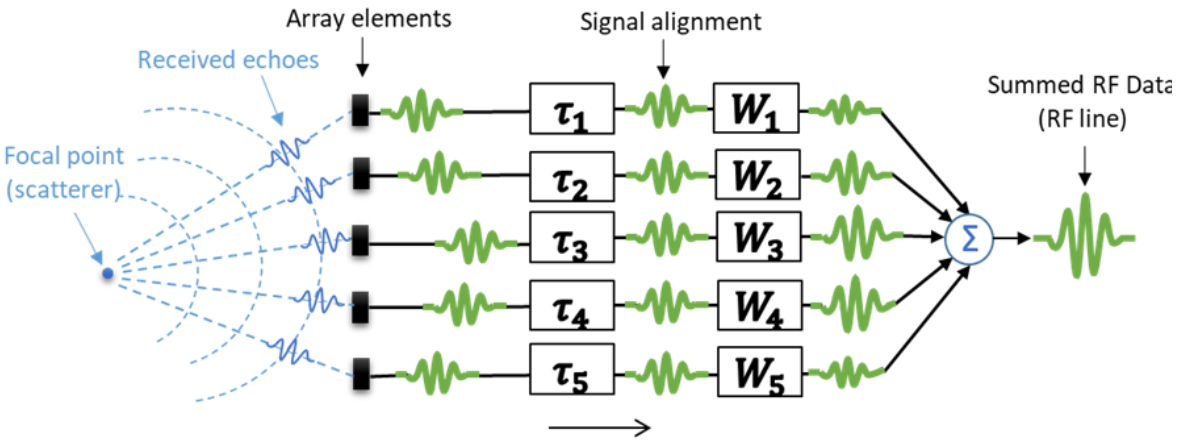

Figure 6. Beamforming principle to produce raw RF data, using 5 element-array. DAS technique includes a summation of the received echoes followed by time alignment and weighting according to the spatial position of the focal point.

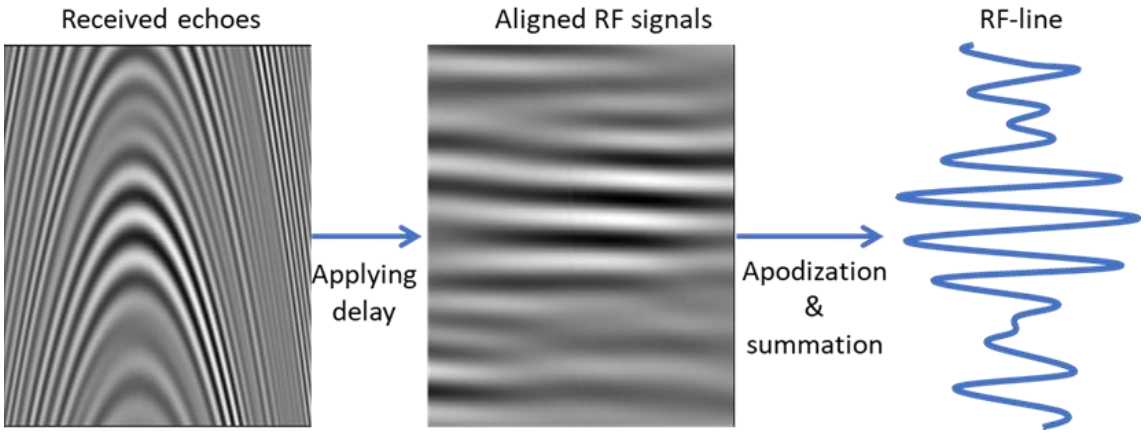

Figure 7. RF data generation with DAS. (a) Gray scale image of the received echoes detected by 64 elements for a single scan line. (b) Time alignment of (a). (c) The summation of all 64 signals forms the RF line.

Mathematically, the RF-line can be expressed as:

$$RF(t) = \sum_{i=1}^{N} W_i y_i(t - \tau_i) \ , \qquad \tau_i = \frac{\left|\vec{r}_c - \vec{r}_f\right| - \left|\vec{r}_i - \vec{r}_f\right|}{c} \ , \tag{14}$$

where N is the number of elements in the array, y_i represents the received echo detected by the i-th element, τ_i is its time delay required for focusing it at the sampled point of interest and W_i is the apodization weight applied on the received y_i echo. $\vec{r}_i$, $\vec{r}_c$, $\vec{r}_f$ are the coordinate vectors (x, y, z) of the i-th element, the element closest to the artificial focus point, and the artificial focal point, respectively, and c is the speed of sound in the medium.

At the end of beamforming, all the RF lines obtained are juxtaposed to one matrix, called the RF image (Figure 8(a)). In order to obtain the final B-mode image, the RF image needs to pass through few further processing stages. The block diagram in Figure 9 depicts the different steps that are usually implemented [34]:

- **Band filtering –** filtering of the high frequencies is required since the frequencies used in diagnostic applications are in the range of several megahertz and therefore lower frequencies than the transmitted signal band may be attributed solely to noise. Regarding the low-pass filtering, this element is needed to further reduce the noise and also to

prepare the signal for digitization by the A/D converter and in particular to limit the maximal frequency in order to avoid aliasing before digitizing according to Nyquist theorem (Figure 8(b)).

- **Envelope detection** - this stage allows to display the changes stemming from the reflecting texture and not from the wave profile. It is usually implemented using the Hilbert transform (Figure 8(c)) while the resulted signals are transformed to gray level values.

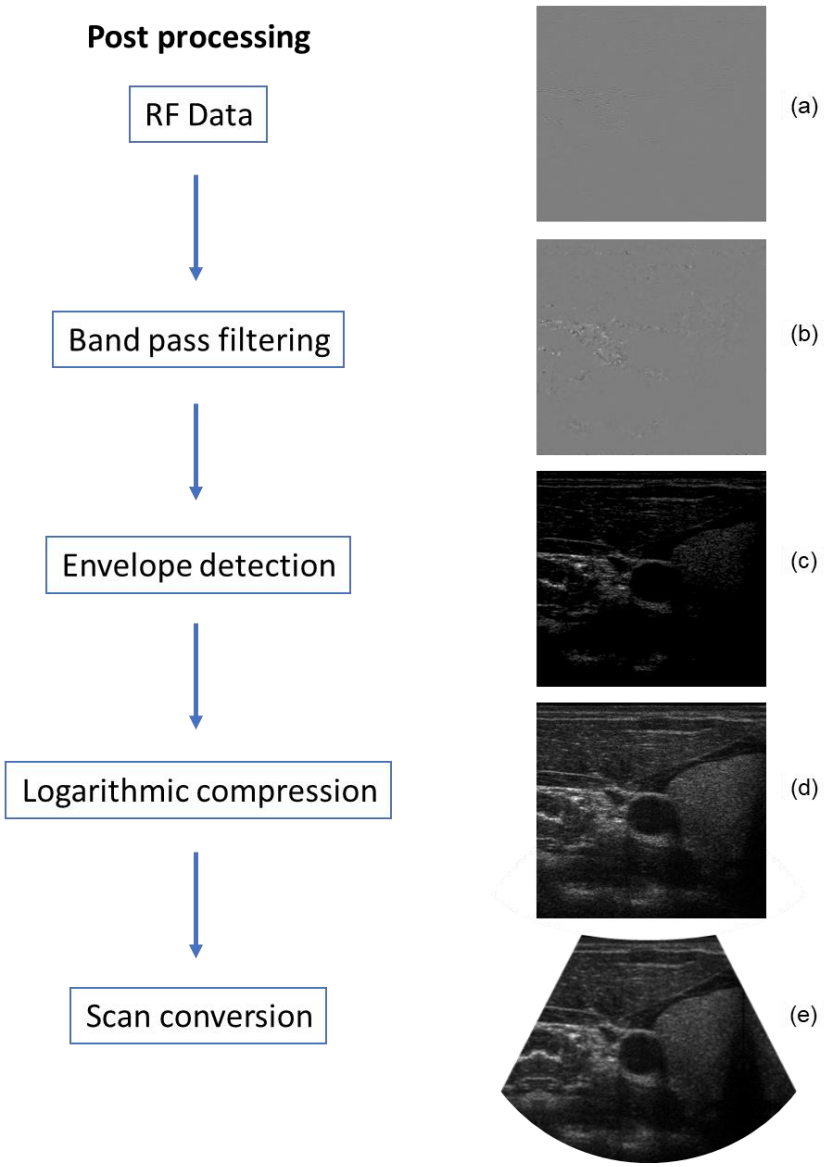

Figure 8. Diagram of typical post-processing stages applied on the RF image to obtain a B mode image. (a) the original RF image, (b) the RF image after band-pass filtering, (c) a gray scale image obtained after envelop detection with Hilbert transform, (d) a gray scale image after logarithmic compression, (e) a fan-shaped image after scan conversion.

- **Logarithmic compression -** diminishes the gaps in contrast between different regions of the image and allows the visualization of both weak and strong reflections in the same image (Figure 8(d)).
- **Scan conversion-** the coordinates of the matrix's pixels obtained until this stage are now transformed to their corresponding coordinates in the imaged region according to the scanning parameter such that the final B-mode image is obtained (Figure 8(e)).

3.5 Successive focusing

One of the limitations of two-way focusing stems from the fact that the signal acquisition along each scan-line is obtained after transmitting only a single focal spot, that is then swept across the field of view. With a single transmission focus, the signal diverges outside of the focal region, i.e., the depth of focus (DOF). Therefore, in practice, the advantages of two way focusing are confined to the focal region, and the lateral resolution and the contrast of an object outside the DOF are significantly degraded. To image a larger DOF, successive focusing is often used, where the transmission focal depth is updated successively with several transmissions [12]. A complete image is then constructed by splicing together the focused area from each of the individual transmissions (Figure 9). While this method yields high resolution and contrast, its main drawback is that the beams of different focal lengths can be transmitted only one by one, and the transmission of the next beam can be done only after all the echoes produced by the previous one returned to the transducer. Otherwise, echoes generated by the reflection of a beam from deeper tissues may arrive at the same time as those produced by the following beam coming from shallower tissues, thus producing a false representation of structures in the image. Therefore, it is obvious that the method's benefits come at the expense of frame rate loss, which is degraded by a factor that equals the number of transmitted foci. Montage using an infinite number of

images focused at different depths would produce an image of the highest quality, however, this would require an infinite amount of time and have a zero imaging frame rate. Therefore, the tradeoff between the frame rate and the image quality should be considered. An ultrasound method that can provide high lateral resolution over a large DOF with enhanced frame rate is desirable for important medical applications including the detection of anatomical landmarks, ultrasound-guided interventions, fetal surgeries, and cardiovascular interventions [13], [35], [36].

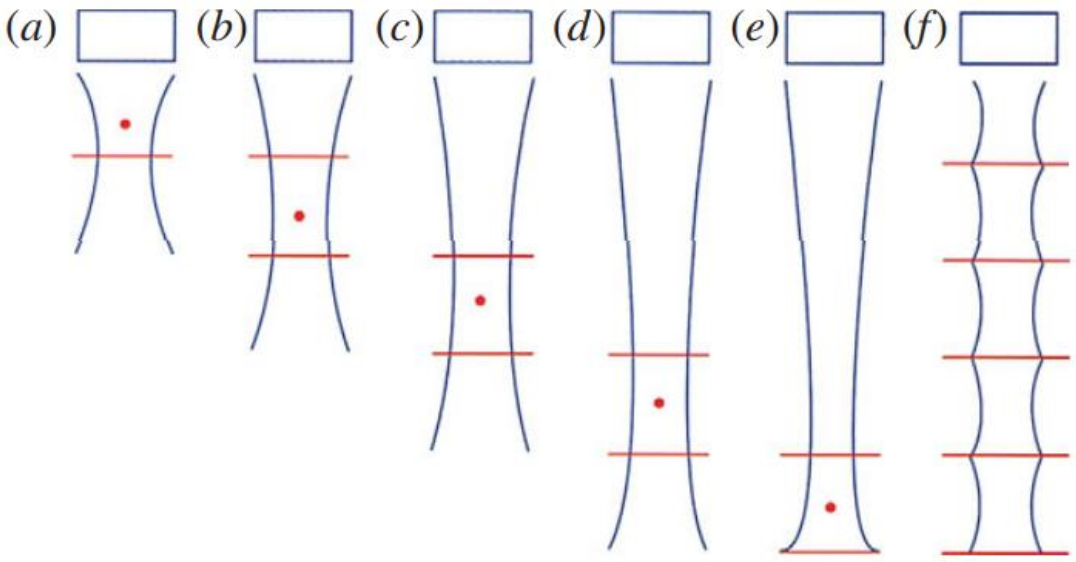

Figure 9. Illustration of successive focusing method for transmission. (a)-(e) progressively deeper focus, (f) the final image constructed by splicing together the focused area from each of the five individual transmissions acquired through single focus at transmission.

3.6 SAMI

Recently, a method for simultaneous axial multifoci imaging (SAMI), based on temporal superposition of axial multifoci waveforms in a single transmission, was developed. It uses temporal superpositioning of multiple waveforms where each wavefront is focused to a different depth. By transmitting the combined waveform, axial multifoci imaging is achieved using a

single acoustical transmit. Thus, an enhanced framerate is obtained compared to successive focusing, while maintaining high lateral resolution and depth of field [1].

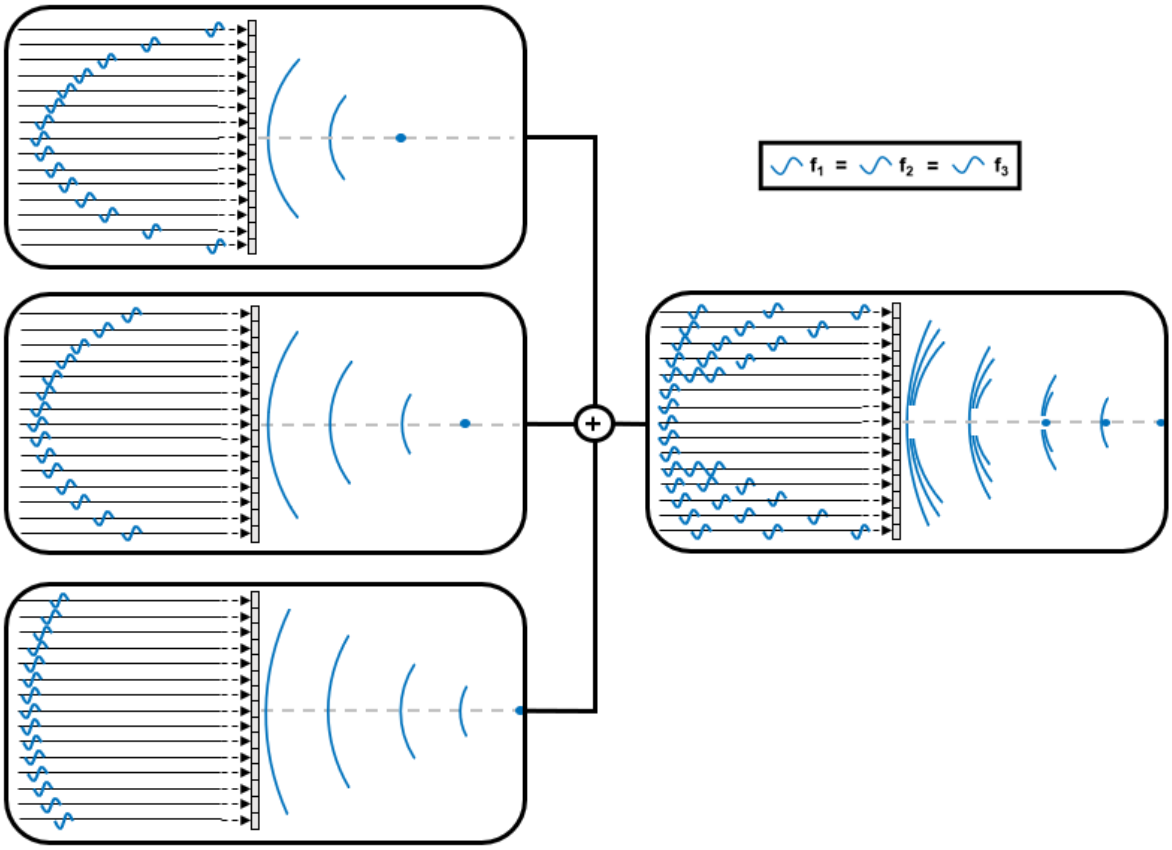

Figure 10. Schematic illustration of the standard SAMI method. Few focused waveforms, each focusing at different depth, are superpositioned into an axial multifoci waveform.

In standard focus transmission, a single focal spot is generated by applying delay in transmission between each transducer's elements such that all the single cycle pulses emitted will interfere constructively, i.e. at the same time and with the same phase, at the focal point predetermined. The longest delay dictates the transmission duration. Since each element transmits only a single cycle, its signal is zero throughout most of the transmission duration – or equivalently, its duty cycle is very low - and therefore, the time domain is not used efficiently. Therefore, by transmitting multiple waveforms in a single transmission, corresponding each to a

different axial focus, the time domain can be exploited more efficiently. A schematic illustration of SAMI, where three axial foci are transmitted simultaneously with constant frequency, is depicted in Figure 10. It should be noted that the central elements of the transducer are not contributing to all the focal spots and the reason for that will be elaborated later, as part of 'design of signal transmission' section.

One of the principal advantages of this method is the fact it can be incorporated in a regular imaging routine, by changing the transmitted signal based on the designed pattern. Moreover, imaging and image reconstruction can be performed by the programmable ultrasound system in real time in a user-friendly manner.

3.7 Lateral resolution, depth of focus & attenuation tradeoff

The point spread function (PSF) of an ultrasound system utilizing two way focusing is the product of the transmit and the receive PSFs [37]–[40]. The SAMI method transmits each focus with the outer elements, while the deepest focus is transmitted with the entire aperture. In this case, the effective aperture diameter remains D and the lateral resolution remains similar to the case where the entire aperture is transmitting. Transmitting with the outer elements contributes to the generation of side lobes, but does not affect the main lobe [1]. For all axial multifoci, the entire aperture is used on receive; thus, the receive aperture also has size D. Since the lateral resolution and the DOF are defined by the transmit and receive aperture diameters, the SAMI method has a similar lateral resolution as standard two way focusing [1]. The lateral resolution is limited by diffraction to length scales according to:

$$FWHM = const \times \lambda_n \frac{z_n}{D} \tag{15}$$

where FWHM is the full width half maximum of the beam, λ_n is the axial focal wavelength, given by c/f_n where c is the sound velocity and f_n is the axial focal frequency, z_n is the distance between the transducer to the specific axial focus, D is the transducer aperture diameter and *const* is a parameter determined by the imaging method and the transducer apodization. For a rectangular aperture and two way focusing *const*=0.886 [5]. This formula is valid for the case where $z_n \geq D$, and the entire aperture can contribute to the focus generation. Lateral resolution decreases as a function of depth; however, for a given depth it increases when increasing the frequency.

Another important parameter is the DOF which defines the axial width around each focus, where the beam is within the full width at half maximum of the beam width, and is approximated by [41]:

$$DOF = 7.1\lambda_n \left(\frac{z_n}{D}\right)^2 \tag{16}$$

The quotient of the focal distance and the aperture diameter is also known as the F-number, such that F# = z/D. The DOF is inversely proportional to the frequency; i.e., increasing the frequency will decrease the DOF. However, the DOF increases quadratically with the focal distance.

Finally, the attenuation of a propagating acoustic wave within a biological tissue is given by [5]:

$$Attenuation\ [dB] = \alpha_{dB} \cdot f_n \cdot z_n \tag{17}$$

where α_{dB}[dB/cm/MHz] is the medium's attenuation coefficient. The attenuation increases as a function of both frequency and depth.

In conclusion, as frequencies increases, resolution improves whereas penetration and DOF decreases (Figure 11). As a result, the trade-offs for use of higher transmitted frequency are reduced tissue penetration and reduced depth of focus. This trade-off between image resolution

and penetration guides the choice of transmitted frequency in clinical imaging [24], [42].

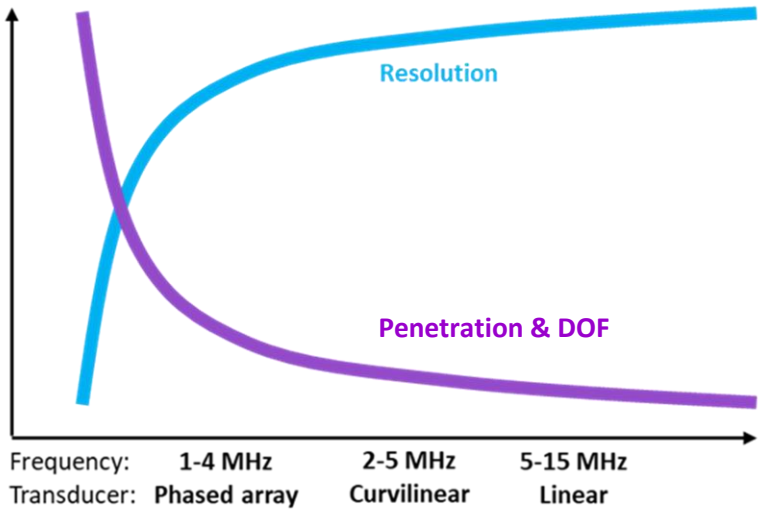

Figure 11. Resolution, penetration and DOF tradeoff

3.8 Proposed method concept

While SAMI is efficient in generating axial multifoci, it is limited by the fact that all of the waveforms are transmitted at a constant frequency. Therefore, this study aimed to optimize standard SAMI by implementing a frequency multiplexed SAMI (FM-SAMI) method. The FM-SAMI proposed here is designed to transmit each waveform at a different frequency such that the generated axial multifoci are frequency-dependent. This optimization was developed to achieve two main objectives that are not feasible using conventional SAMI. On one hand, by transmitting the lowest frequency to the shallowest focus, and gradually increasing the frequency as a function of depth (i.e. “FM-SAMI Increasing”), a more uniform lateral resolution across the entire field of view can be achieved. In particular, since standard SAMI uses the entire aperture for transmit, F-number adjustment by changing the effective aperture size is not feasible, and hence constant lateral resolution as a function of depth cannot be obtained. Here, by changing

each focus frequency, a more uniform lateral resolution as a function of depth becomes feasible. Alternatively, by gradually decreasing the frequency as a function of axial multifoci, high lateral resolution at shallow depths along with enhanced penetration for the deeper depths can be obtained (i.e. “FM-SAMI Decreasing”). Figure 12 presents a schematic illustration of the proposed method, and more specifically of the 'FM-SAMI Increasing'.

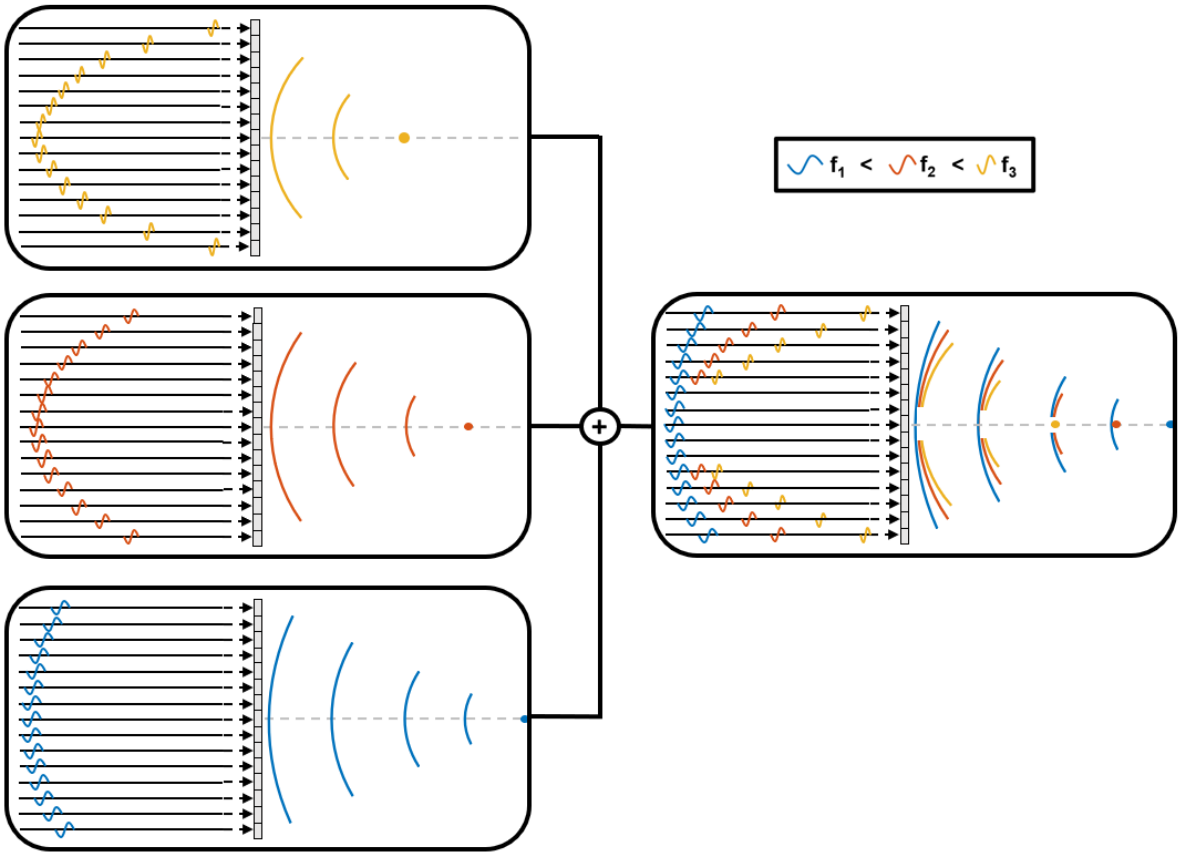

Figure 12. Schematic illustration of the proposed method. Few focused waveforms, each focusing at different depth, are superpositioned into a frequency multiplexed axial multifoci waveform where the transmitted frequency is depth dependent.

The FM-SAMI method is implemented in real-time and tested experimentally using an advanced programmable ultrasound system that can dynamically modify the transmitted pulses for each transducer element separately using a built-in arbitrary waveform generator [14], [15].

4 Materials and methods

Standard SAMI uses a superposition of multiple waveforms such that their simultaneous transmission generates axial multifoci in a single acoustical transmit event, thus increasing the frame rate (Figure 13(a)) [1]. However, since all the waveforms are transmitted at a constant center frequency, there is a tradeoff between attenuation and lateral resolution when choosing a constant frequency for all the axial depths. The frequency multiplexed SAMI (FM-SAMI) method makes it possible to transmit each superpositioned waveform at a different frequency so that the generated axial multifoci are frequency-dependent.

For this purpose, the first milestone was to understand, theoretically, what could be the benefit of combining frequency dependence together with the existing SAMI method. Then, the next milestone was to properly engineer the custom matrix excitation that determines the signal transmitted by the transducer and superposition waveforms with varying frequencies, such that axial multifoci with depth-dependent frequency at the desired depths will be achieved. Subsequently, hydrophone experiments were performed in order to better understand how the acoustic fields obtained looked and ensure that these matched the expected patterns and in particular, that the foci generated were obtained at the proper depths. Finally, the last milestone was to perform US experiments, including setup design and programming the US system to implement the optimized imaging technique, in order to validate the method and compare the performance of its both versions – i.e. FM-SAMI Increasing and Decreasing - to those of the standard SAMI.

4.1 Design of the transmission signal

FM-SAMI uses a superposition of multiple waveforms that correspond to different axial foci

such that their simultaneous transmission generates frequency-dependent axial multifoci in a single acoustical transmit event. This multiline transmit method uses the time domain more efficiently by transmitting multiple waveforms that correspond to lateral multifoci in a single transmit event.

However, the implementation of such multiline method for axial multifoci yields to a significant number of elements whose waveforms, corresponding to different foci, overlap. For each element, overlapping waveforms are defined as adjacent waveforms that the distance between them is less than their average pulse length. When designing the superpositioned waveform, the overlap is eliminated (red dashed square, Figure 13(a)). There are two main motivations for removing these overlapping waveforms. First, the overlapping waveforms forms high frequencies area that can't be transmitted by the transducer. Second, this overlap results in a reduced signal compared to successive focusing transmission since the superposition of overlapping waveforms will increase the maximal transmitted intensity. As a result, the other waveforms that don't overlap will be scaled down by a factor corresponding to the number of foci in the sequence, so that the sum of the waveforms will not exceed the piezoelectric maximal element response.

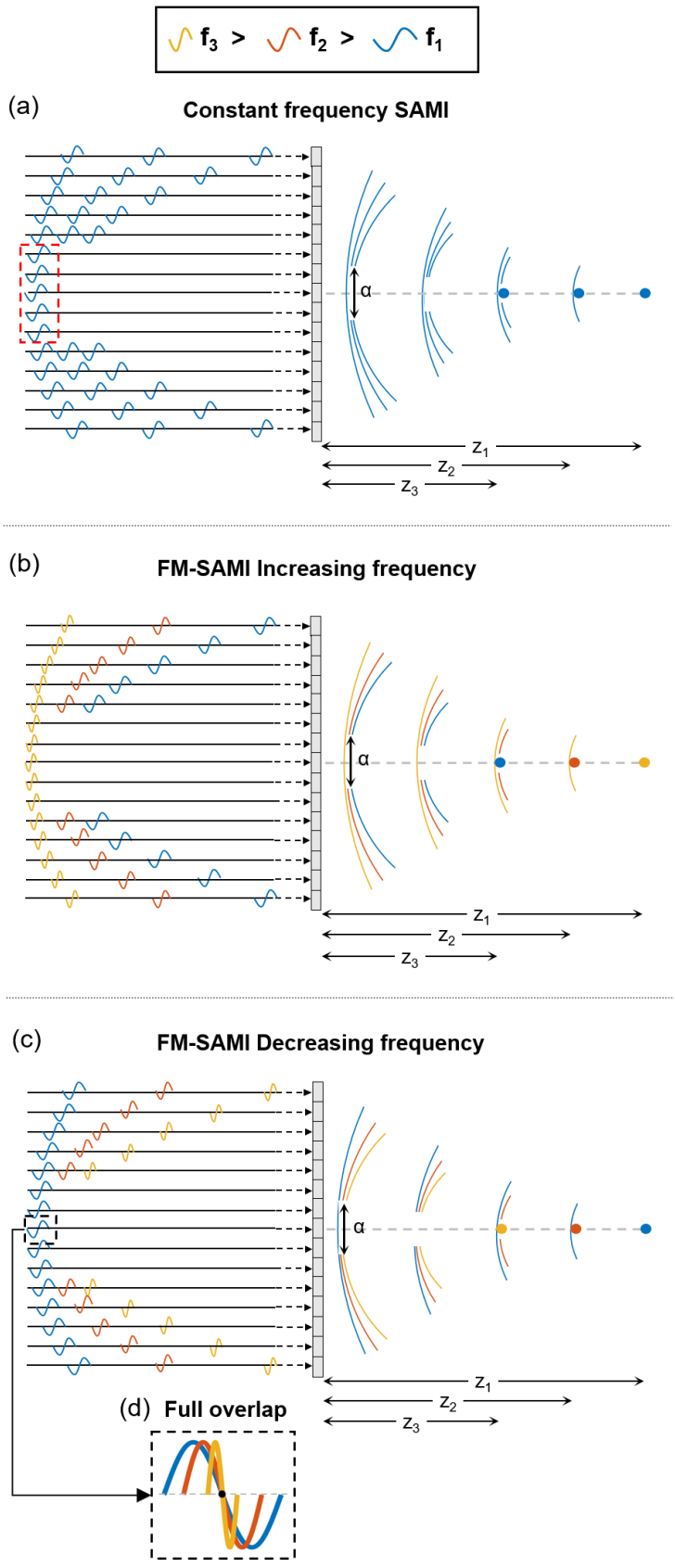

Figure 13. Schematic illustration of the transmission matrices used to generate three axial multifoci using the SAMI and FM-SAMI methods. Each waveform color encodes their center frequency. f_1 (blue), f_2 (orange), and f_3 (yellow) are the lowest to highest transmitted frequencies, respectively. Transmission matrix illustration for (a) Constant frequency SAMI. (b) FM-SAMI with an increasing frequency as a function of depth. (c) FM-SAMI with a decreasing frequency as a function of depth. (d) Illustration of the definition of maximal waveforms overlap.

In order to overcome these issues, the super-position of waveforms is performed only for those that are not overlapping such that aliasing is prevented while assuring the waveform can be transmitted by the transducer. When the matrix transmission is designed, the waveforms corresponding to the deepest focus are initially added to the transmission matrix. Then, the waveforms corresponding to the shallower foci are superpositioned sequentially for all of the elements, except the elements whose waveforms overlap. In the case of overlap, the overlapping elements in the waveform are set to zero (such that these elements transmit only the deeper foci added so far). The process repeats until all of the desired waveforms are superpositioned. Generally, the most significant overlap is that of the central elements, and it gradually reduces for external elements (Figure 13). According to that, only the waveform focused to the deepest depth will be transmitted with the entire aperture whereas the shallower foci will be transmitted with some outer portions of the transducer aperture. Moreover, a constant maximal amplitude is used for all the elements in all waveforms to maximize the transmitted energy.

There are two key features of the combined waveform design. The first is the definition of maximal overlap. The maximal overlap occurs when the waveforms' center coincides (Figure 13(d)). The second feature is the definition of the minimal distance between overlapping waveforms. In order to avoid the overlap between the superpositioned waveforms, an average wavelength is defined as the average wavelength between two successive wavefronts:

$$\lambda_{avg} = \frac{\lambda_{n+1} + \lambda_n}{2} \tag{18}$$

where λ is the wavelength, n is the focus index, such that n=1 represents the deepest focus, n=2 is the second deepest focus, etc. For example, if 3 foci are generated, n=1 is the deepest focus, n=2 is the intermediate focus and n=3 is the shallowest focus. This index notation is used

consistently throughout this paper. In the case where the distance between adjacent waveforms is less than λ_{avg}, the excitation corresponding to the shallowest focus of the two in the superpositioned waveform is set to zero.

Practically, the generation of the focused waveforms is implemented based on the geometrical approach of electronic focusing. According to equation (12) from section 3.3, given that the origin is defined as the center of the central element – which is also the closest element to the focal spot located in its axial direction at $(0,0,z)$, the negatively signed time delay required for the transmission of any element, located at $(x,0,z)$, in order to interfere constructively at the focal location is given by:

$$\tau(x,0,z) = \frac{z - \sqrt{z^2 + x^2}}{c} \tag{19}$$

For each superpositioned waveform, α is a parameter, that is measured from the center of the transducer and represents the aperture size whose elements are set to zero to eliminate adjacent waveform overlap, such that $0 \leq \alpha \leq D$, where D is the full aperture diameter (Figure 13). When defining the origin as the center of the transducer aperture, the element location at which the additional superpositioned waveform transmission begins is denoted by $\pm\alpha/2$. For example, if the additional waveforms use half of the total transmitting aperture, such that the two outer quarters of the transducer elements transmit, then $\alpha=D/2$. Alternatively, generating a focal point that uses 32 elements out of the total 128 array elements yields an $\alpha=3D/4$; i.e., the two outer eighths of the transducer aperture are used for transmit.

It should be of interest to relate between the system parameters and the minimal axial distance enabled between generated foci. The minimum time delay difference between the transmission of two adjacent waveforms is that of the element at which the additional superpositioned

waveform transmission begins, located at x=±α/2. It is equal to $\lambda_{avg}N/c$, where λ_{avg} is the average wavelength between the two successive wavefronts and N is the number of transmitted cycles. Mathematically, it can be written as :

$$\tau\left(\pm\frac{\alpha}{2},0,z_n\right)-\tau\left(\pm\frac{\alpha}{2},0,z_{n+1}\right)=\frac{\lambda_{avg}N}{c} \tag{20}$$

where z_n is the deeper focus depth, z_{n+1} is the adjacent shallower focus, λ_{avg} is the average wavelength according to (18) and N is the number of cycles transmitted. In the case of constant frequency SAMI, $\lambda_{avg}=\lambda$. By substituting in (19) the coordinates indicated in (20), we obtain:

$$z_n-\sqrt{z_n^2+\left(\frac{\alpha}{2}\right)^2}-z_{n+1}+\sqrt{z_{n+1}^2+\left(\frac{\alpha}{2}\right)^2}=\lambda_{avg}N \tag{21}$$

This can be rewritten as:

$$z_n-z_n\sqrt{1+\frac{\alpha^2}{4z_n^2}}-z_{n+1}+z_{n+1}\sqrt{1+\frac{\alpha^2}{4z_{n+1}^2}}=\lambda_{avg}N \tag{22}$$

While this equation can be solved numerically, using the Taylor approximation $\sqrt{(1+x)} \approx 1+x/2$, it can be simplified to an analytic form, which provides a useful tool:

$$z_{n+1}\cong z_n\left(1+\frac{8\lambda_{avg}Nz_n}{\alpha^2}\right)^{-1} \tag{23}$$

Figure 14 presents the combined waveforms for the standard ‘SAMI’, ‘FM-SAMI Increasing’ and ‘FM-SAMI Decreasing’. The parameters were chosen to match those of the P6-3 (Philips, Bothell, WA, USA) phased array transducer that was used in the experiments. The number of cycles was N=1, the number of elements was 128, the aperture diameter was D=27.9 mm, the parameter alpha was set to α=D/2, and the deepest focus was designed to be located at a depth of

z_1 = 100 mm for all of the methods. The superpositioned waveform consisted of 3 axial foci in total (Figure 14). In all these matrices, each parabolic waveform was composed of a white line representing the waveform's positive phase and a black line representing its negative phase. A further maximization of the transmitted energy can be achieved by transmitting waveforms with half cycles instead of full cycles for elements where an overlap in the waveforms exists. After superpositioning all of the waveforms that include a single cycle, half cycles are added based on (23). This is represented by the waveform part that is composed of the white line alone. In the experimental results section, two different α values are presented. α_1 corresponds to the α value obtained when transmitting single-cycle waveforms and $\alpha_{1/2}$ corresponds to transmitting half-cycles, where $\alpha_{1/2} < \alpha_1$. In addition, the more parabolic the wavefront, the shallower is the focus. Therefore, the waveform transmitted with all the elements is the deepest focus. The waveforms used in this work were designed in MATLAB (version 2018a, MathWorks, Natick, MA, USA).

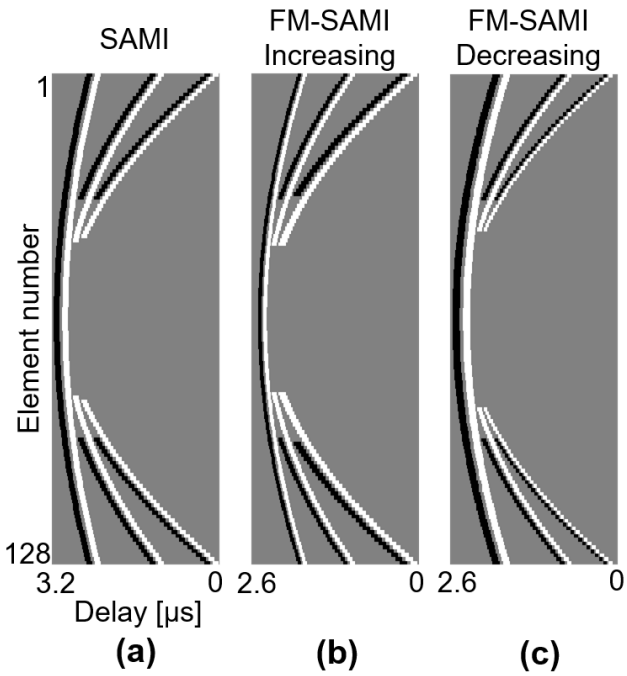

Figure 14. Combined three axial multifoci transmission waveform matrices for a constant α=D/2. Axes are common to all subfigures. (a) SAMI with a constant frequency of 3 MHz. Foci are located at 100, 32.5, 19.4 mm. (b) FM-SAMI with increasing frequency. Foci are located at 100, 45.1, 25.6 mm, for center frequencies of 6, 4.5 and 3 MHz, respectively. (c) FM-SAMI with decreasing frequency. Foci are located at 100, 37.2, 25.6 mm, for center frequencies of 3, 4.5 and 6 MHz, respectively.

In this work, to maximize the range of frequencies used, we chose to utilize the entire transducer's bandwidth and selected evenly spaced frequencies within its bandwidth (3, 4.5, and 6 MHz) in either an increasing or decreasing order. For a constant frequency SAMI, a center frequency of 3, 4.5 or 6 MHz was chosen for all 3 axial multifoci. Note that since (23) is wavelength dependent, the location of the two shallowest foci changes across different methods for a constant α parameter. For the standard SAMI, at a constant frequency of 3 MHz, the foci's locations based on (23) were z_1=100 mm, z_2=32.5 mm and z_3=19.4 mm (Figure 14(a)). For 'FM-SAMI Increasing', the foci depths were z_1=100 mm, z_2=45.1 mm and z_3=25.6 mm (Figure 14(b)). As expected, the wavefront for the deepest focus has the thinnest lines, indicating a higher frequency of 6 MHz compared to the shallowest focus that has a center frequency of 3 MHz. 'FM-SAMI Decreasing' shows the opposite trend, where the thinnest wavefront is the shallowest focus that was transmitted at a center frequency of 6 MHz, while the deepest focus was transmitted at a frequency of 3 MHz. The foci locations for this case were z_1=100 mm, z_2=37.2 mm and z_3=25.6 mm (Figure 14(c)).

Theoretically, and according to equation (15) presented in section 3.7 that defines the FWHM obtained in two-way focusing, in order to achieve uniform lateral resolution as a function of depth; i.e., constant FWHM, a transducer with a bandwidth proportional to the range scanned should be used, and the transmitted frequency should increase linearly as a function of depth, as in 'FM-SAMI Increasing'. The change in frequency as a function of depth can be described by:

$$f_{n+1} = f_n \cdot \frac{z_{n+1}}{z_n} \tag{24}$$

where n=1 is the deepest focus, and f_n is the higher frequency transmitted to the deepest focus (out of each pair of adjacent foci) at a distance of z_n. This relationship indicates that in order to obtain a uniform lateral resolution, the transducer bandwidth dictates the distance between the

nearest and deepest foci. For example, in order to achieve uniform lateral resolution with the P6-3 transducer while exploiting its entire bandwidth, the shallowest focus should be generated with a frequency of 3 MHz and the deepest focus should have a frequency of 6 MHz. Based on (24), the distance to the deepest focus should be twice the distance to the shallowest focus.

Whereas 'FM-SAMI Increasing' is aimed to achieve a more uniform lateral resolution for all foci, 'FM-SAMI Decreasing' is aimed to maximize the lateral resolution for the shallowest foci, while minimizing attenuation for the deepest foci by gradually decreasing the transmitted focal frequency as a function of depth.

Similarly to lateral resolution and based on the attenuation equation (17) described in section 3.7, in order to obtain uniform attenuation as a function of the focal depth, the frequency should decrease proportionally according to:

$$f_n = f_{n+1} \cdot \frac{z_{n+1}}{z_n} \tag{25}$$

where n=1 is the deepest focus, and f_n is the lower frequency transmitted to the deepest focus (out of each pair of adjacent foci) at a distance of z_n. For example, in order to achieve uniform attenuation as a function of depth with the P6-3 transducer while utilizing its entire bandwidth, the shallowest focus should be generated with a frequency of 6 MHz and the deepest focus should have a frequency of 3 MHz. In addition, the distance to the deepest focus should be twice the distance to the shallowest focus.

In a practical scenario, the user determines the focal depths empirically, based on the features that exist in the scanned sample, and not based on a constant α. α can be isolated from (23) and be calculated by:

$$\alpha = \pm\sqrt{8\lambda_{avg}N\left(\frac{1}{z_{n+1}} - \frac{1}{z_n}\right)^{-1}} \tag{26}$$

4.2 Ultrasound experiments

This stage includes designing the setup and programming the US system to perform the desired imaging protocol, considering the chosen US transducer and excitation parameters. Experiments were performed using a phased array sector transducer, P6-3 (Philips, Bothell, WA, USA), composed of 128 elements with a pitch of 0.22 mm (Figure 15(a)). A programmable ultrasound system (Vantage 256, Verasonics Inc., Kirkland, WA, USA) was used in all the experiments (Figure 15(b)). The superpositioned waveforms were transmitted using the arbitrary waveform generator (AWG), a feature in the programmable ultrasound system which enables the transmit of custom waveforms. On receive, the beamforming was performed by the built-in beamformer, and the reconstructed ultrasound images were displayed in real time.

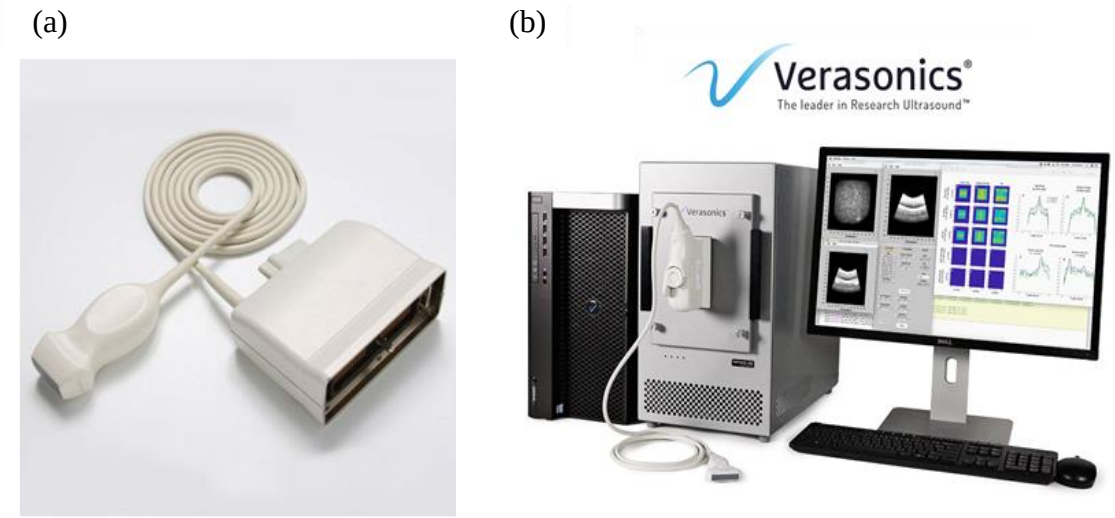

Figure 15. Hardware used in ultrasound experiments: (a) P6-3 phased array and (b) Verasonics programmable research ultrasound system.

4.2.1 Hydrophone setup

A needle hydrophone with an aperture of 0.2 mm was used to measure the emitted pressure fields that were transmitted by the P6-3 transducer. The hydrophone probe was positioned perpendicularly to the emitted field inside a degassed water tank, and mounted on a three-dimensional positioning system (Newport motion controller ESP 300), (Figure 16). The pressure signals received by the hydrophone were recorded by a digital oscilloscope (MDO3024, Tektronix, OR, USA), and saved for offline processing.

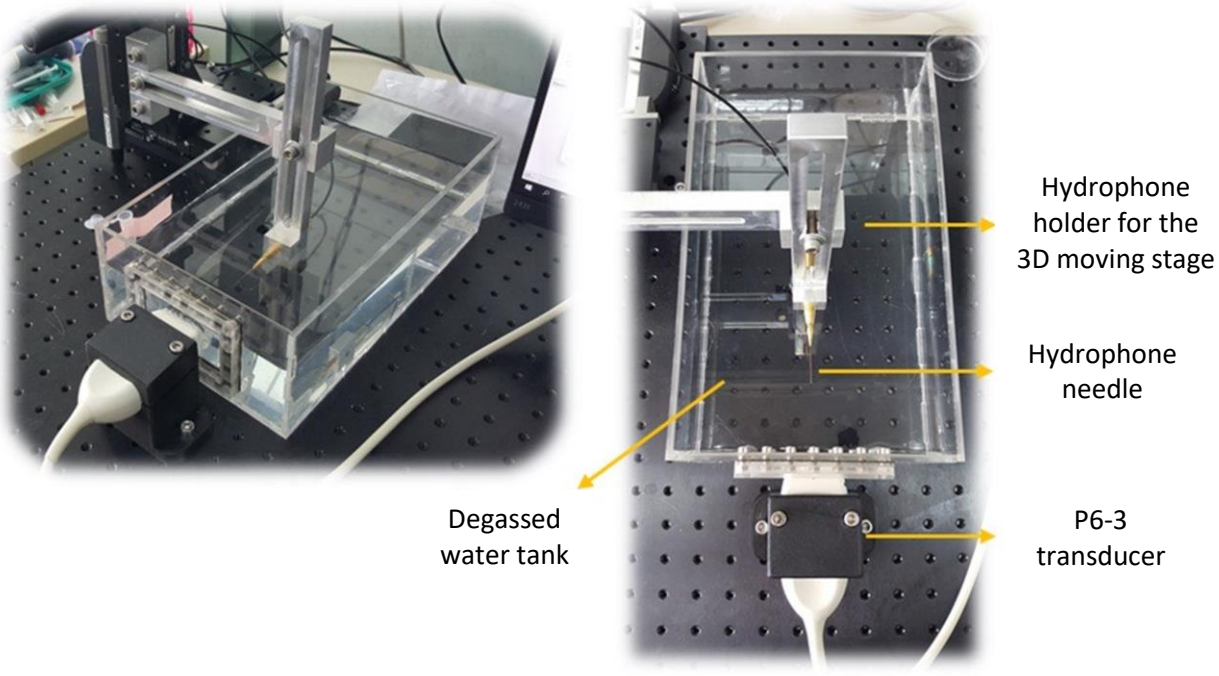

Figure 16. Hydrophone set-up used for the measurement of the acoustic fields generated by the P6-3 transducer.

4.2.2 Resolution experiment's setup

Lateral resolution experiments were performed in the degassed water tank by imaging a sector of 45° with an angular precision of 0.18° obtained by scanning along 256 scan lines [43]. The resolution target was composed of five 50 µm nylon wires that were axially spaced at equal intervals of 10 mm in a depth range of 30 to 70 mm (Figure 17).

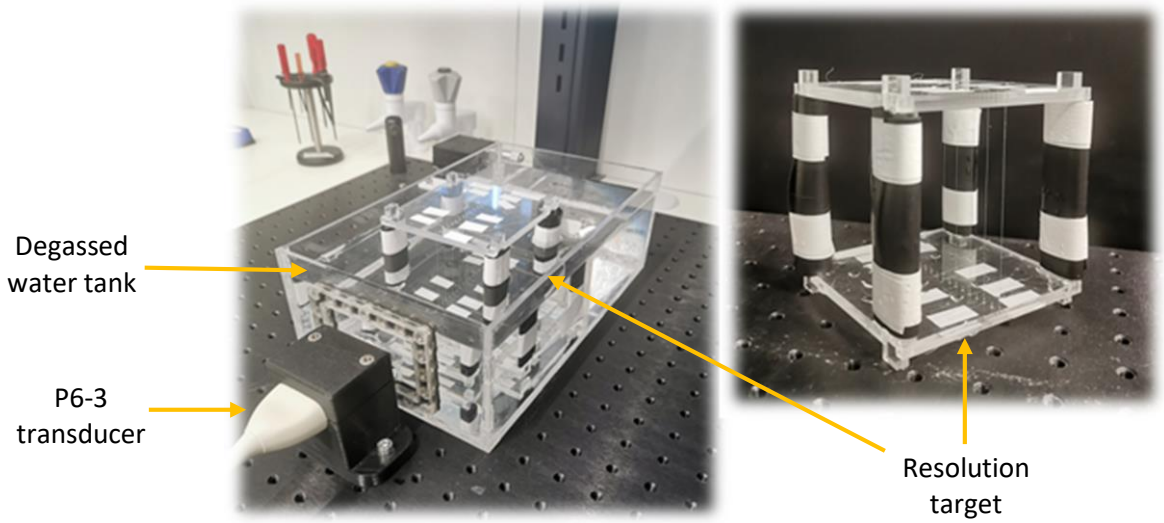

Figure 17. Target resolution set-up used in the resolution experiments including P6-3 transducer, degassed water tank and resolution target composed of nylon wires.

4.2.3 Contrast experiment's setup

The method's contrast was evaluated by imaging cysts at fixed depths within a commercial tissue-mimicking phantom (CIRS 040GSE, Virginia, USA) consisting of a Zerdine® hydrogel polymer [44] (Figure 18). This phantom has an attenuation factor of 0.5 dB/cm/MHz, and includes homogenous specular reflectors. Similar to the resolution experiments, the P6-3 transducer was used for the imaging. Images were acquired by a 22.5° sector scanned with 128 scan lines, resulting in the same angular precision as used in the resolution experiments.

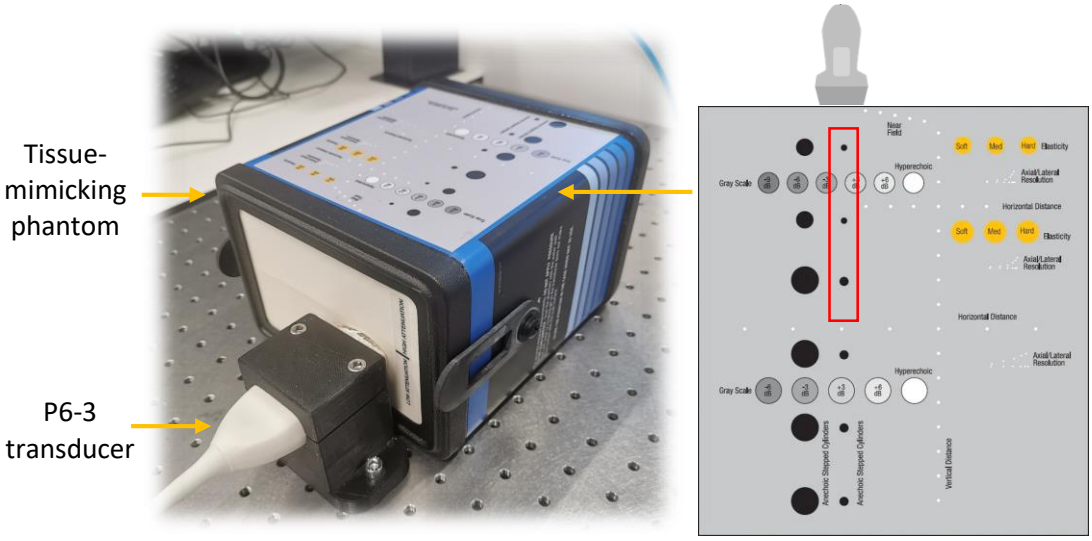

Figure 18. Contrast experiments' set-up including P6-3 transducer and tissue-mimicking phantom. The target layout within the phantom is illustrated while the area containing the cysts used for the measurements is marked on it by the red rectangle.

5 Results

5.1 Theoretical simulation results

Numerical simulations were conducted in Matlab to assess the effect of the different parameters on the obtained DOF, lateral resolution and attenuation using constant frequency SAMI, and FM-SAMI (Increasing and Decreasing frequency). The methods were compared for the generation of three axial multifoci, such that the deepest focus was at 100 mm. The simulation parameters matched those of the P6-3 transducer that was used in the experimental results and included transmitting the axial multifoci at frequencies of 3, 4.5 and 6 MHz (Figure 19). For each of the SAMI and FM-SAMI methods, the foci depths were chosen based on (23) such that α was constant and equaled D/2. For this case, the foci locations varied for each method. Figure 19(a)-

(c) presents the DOF obtained for each focus as a function of frequency. The DOF of each focus point is indicated by a horizontal segment whose color encodes the transmitted frequency. The frequencies are also indicated on the y-axes. In standard SAMI, the DOF for 3 constant frequencies is compared (3, 4.5 and 6 MHz) (Figure 19(a)). Since $\alpha = D/2$, the shallowest focus at 6 MHz is at a distance of 32 mm, compared to a distance of 19 mm for a center frequency of 3 MHz. For the deepest focus at 100 mm, the DOF of the 3 MHz is larger than that of the 6 MHz, as expected. Thus, lower frequencies yield lower focus density, but provide a larger DOF. For 'FM-SAMI Increasing' (Figure 19(b)), and 'FM-SAMI Decreasing' (Figure 19(c)), both the deepest focus (z=100 mm) and the shallowest focus (z=26 mm) co-align, whereas the intermediate focus depth location varies across methods (z=45 mm when increasing the frequency compared to z=37 mm when decreasing the frequency). Since the DOF decreases when increasing the frequency, at the deepest focus, the 'FM-SAMI Decreasing' DOF is larger than that of 'FM-SAMI Increasing', with the opposite trend for the shallowest focus. Note that 'FM-SAMI Decreasing' yields a nearly continuous DOF (Figure 19(c)). Therefore, one of the advantages of combining frequency multiplexing with SAMI is that a more continuous DOF can be obtained by adapting the transmitted frequency for each focus.

The theoretical lateral resolution for each of the axial multifoci in Figure 19(a)-(c) was calculated based on the FWHM from (15) (Figure 19(d)). Since the focal locations are determined by a constant $\alpha=D/2$, a uniform lateral resolution is not obtained for 'FM-SAMI Increasing'. For 'FM-SAMI Decreasing', the lateral resolution at the shallowest depth is maximized, while the DOF for the deepest focus is enhanced (Figure 19(c)).

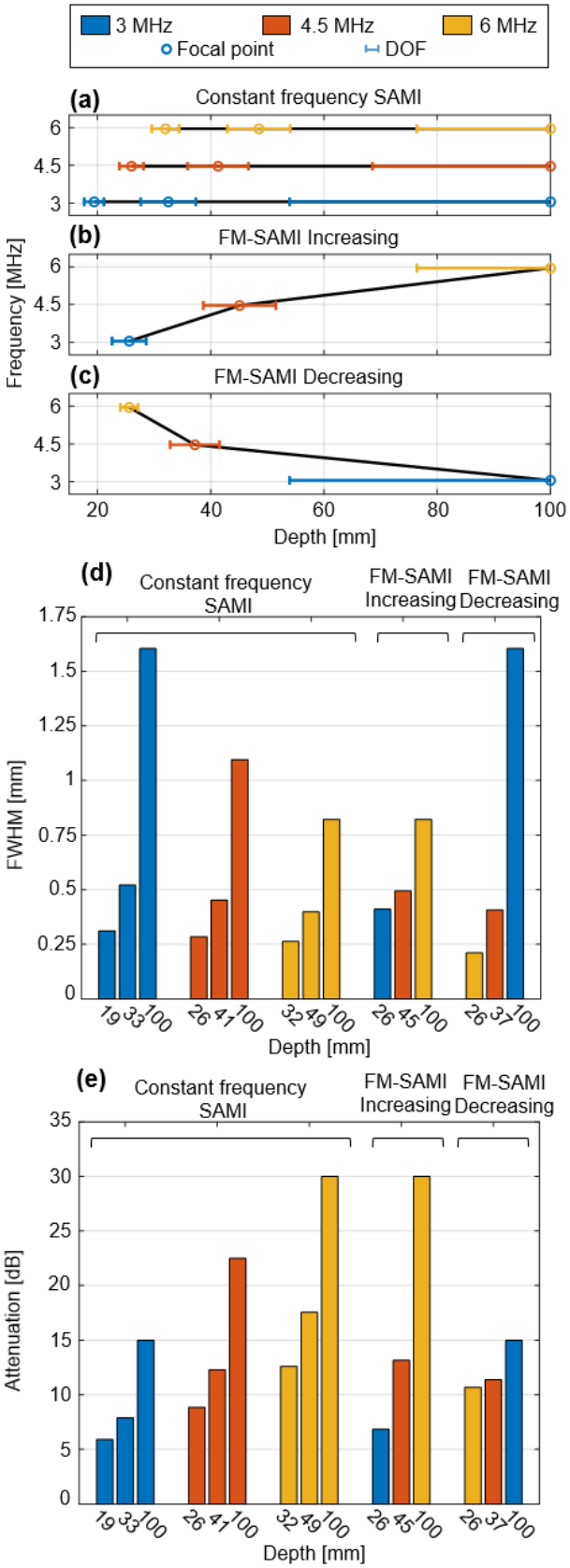

Figure 19. Simulation results for simultaneous generation of 3 axial multifoci. (a) Constant frequency SAMI at 3, 4.5 or 6 MHz. (b) FM-SAMI with increasing frequency from 3 to 6 MHz as a function of depth. (c) FM-SAMI with decreasing frequency from 6 to 3 MHz as a function of depth. The DOF is indicated by the horizontal lines in (a)-(c). (d) FWHM for each focal spot in (a)-(c), respectively. (e) Attenuation for each focal spot in (a)-(c), respectively. The different colors of the horizontal segments in (a)-(c) and the vertical bars in (d) and (e) encode the transmitted frequency, with 3 MHz (blue), 4.5 MHz (orange), and 6 MHz (yellow).

The theoretical attenuation values for each of the axial multifoci in Figure 19(a)-(c) were calculated based on (17) using an attenuation coefficient of 0.5 dB/cm/MHz, which is a standard value for soft tissues. Since the two shallower foci for each of the methods were transmitted with half the elements, additional 3 dB attenuation were added to their predicted attenuation.

5.2 Experimental results

Experiments using the different SAMI methods were conducted in hydrophone scans and resolution targets in a water tank to characterize the emitted acoustic fields and the lateral resolution, in cyst targets embedded within a tissue mimicking phantom to assess the resulting contrast and in an ex-vivo turkey breast.

5.2.1 Hydrophone measurements

Validation of the theoretical estimations was carried using hydrophone measurements of the emitted acoustic pressure fields according to the setup described in section 4.2.1. Constant frequency SAMI at 3, 4.5 and 6 MHz, 'FM-SAMI Increasing' and 'FM-SAMI decreasing' were used to generate 3 axial multifoci at depths of 30, 50 and 70 mm (Figure 20). In this work, to maximize the range of frequencies used, we chose to utilize the entire transducer's bandwidth and selected evenly spaced frequencies within its bandwidth (3, 4.5, and 6 MHz). The foci used here were chosen such that the shallow distance was 30 mm that equals approximately to the aperture diameter. The choice of additional foci at 50 and 70 mm was done to enable an equal spacing of 20 mm between each focus, and utilize significant enough transmitting elements to generate the axial multifoci.

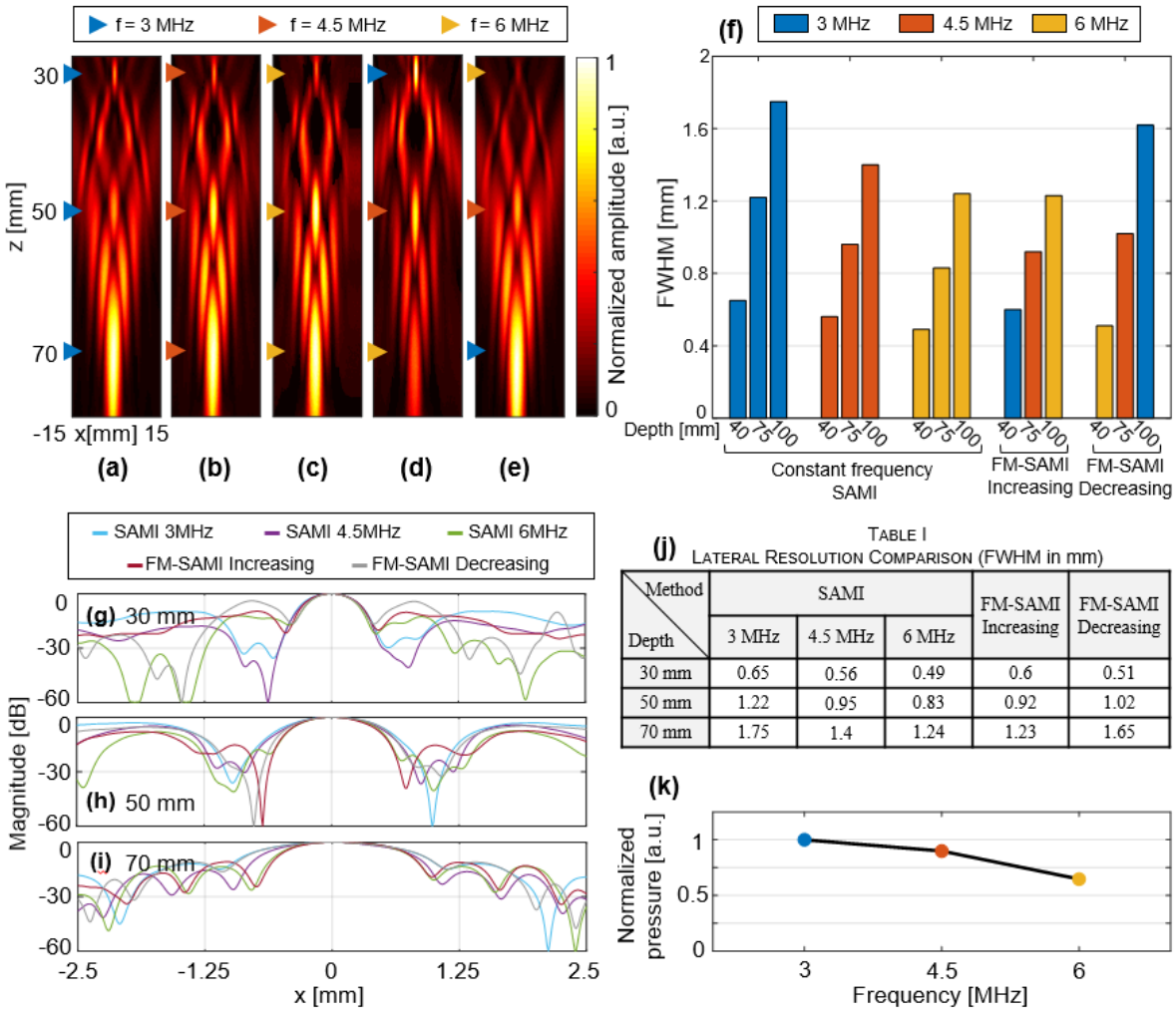

TABLE I
LATERAL RESOLUTION COMPARISON (FWHM in mm)

Method / Depth	SAMI 3 MHz	SAMI 4.5 MHz	SAMI 6 MHz	FM-SAMI Increasing	FM-SAMI Decreasing
30 mm	0.65	0.56	0.49	0.6	0.51
50 mm	1.22	0.95	0.83	0.92	1.02
70 mm	1.75	1.4	1.24	1.23	1.65

Figure 20. Hydrophone measurements of the emitted acoustic pressure fields. Constant frequency SAMI (a) 3 MHz. (b) 4.5 MHz, and (c) 6 MHz. (d) 'FM-SAMI Increasing' from 3 to 6 MHz. (e) 'FM-SAMI Decreasing' from 6 to 3 MHz. Axes are common to (a)-(e) and (g)-(i). (f) FWHM for each focal spot in (a)-(e). (g)-(i) Lateral cross sections of the PSFs obtained at the different focal depths (30, 50, 70 mm) in (a)-(e) for each method, respectively. (j) Table I summarizing the FWHM values from (f). (k) Normalized frequency response of P6-3 transducer sampled at 3, 4.5 and 6 MHz.

The lateral resolution, as quantified by the FWHM, followed a similar trend as in the simulation results (Figure 20(f)-(j)). For the shallowest depth at 30 mm, the FWHM was reduced by a factor of 1.3 'FM-SAMI Decreasing', compared to the constant 3 MHz SAMI and 'FM-SAMI Increasing' method. The FWHM of each frequency component in the 'FM-SAMI Increasing' and 'FM-SAMI Decreasing' was similar to its corresponding frequency component in the

constant frequency SAMI counterpart. For the deepest depth at 70 mm, the FWHM was reduced by a factor of 1.4 for the 'FM-SAMI Increasing' method that transmits 6 MHz, compared to the 'FM-SAMI Decreasing' method. The results are summarized in Table I (Figure 20(j)). Lateral cross sections for each depth show the presence of side lobes for each SAMI method (Figure 20(g)-(i)). This occurs due to the fact that only the outer elements are used for the shallow foci generation at 30 and 50 mm, compared to 70 mm that is generated using all of the elements. Since the two-way PSF is the product of the transmitted field and the entire aperture on receive, the sidelobes are significantly reduced in the two-way PSF, as will be demonstrated in the next section of resolution target experiments. In addition, the transducer frequency response, for the three frequencies used here (3, 4.5 and 6 MHz), was evaluated (Figure 20(k)). From these measurements, the 3 MHz frequency has the strongest frequency response, and it drops by 10% and 35% for the 4.5 and 6 MHz, respectively. Therefore, all of the three frequencies used are within 3 dB of the maximal frequency response.

5.2.2 Resolution targets experiments

Lateral resolution experiments were performed in the degassed water tank according to the setup described in section 4.2.2. Three axial multifoci were generated with each method at 30, 50 and 70 mm, using the same parameters used for the hydrophone measurements. The lateral resolution, as quantified by the FWHM, followed a similar trend as in the simulation results (Figure 21). For the shallowest depth at 30 mm, the FWHM was reduced by a factor of 1.7 for the 'FM-SAMI Decreasing' method that transmits 6 MHz compared to the 3 MHz constant frequency SAMI and 'FM-SAMI Increasing' methods that yield the same FWHM. For the intermediate focus at 50 mm, all methods yielded a similar FWHM, since all methods transmit 4.5 MHz for this focus. This FWHM is narrower than the FWHM of the constant frequency

SAMI that transmits a frequency of 3 MHz, and wider than the FWHM of 6 MHz constant frequency SAMI. For the deepest depth at 70 mm, the FWHM was reduced by a factor of 1.25 for the 'FM-SAMI Increasing' method that transmits 6 MHz, compared to the 3 MHz constant frequency SAMI and 'FM-SAMI Decreasing' methods that yielded a similar FWHM.

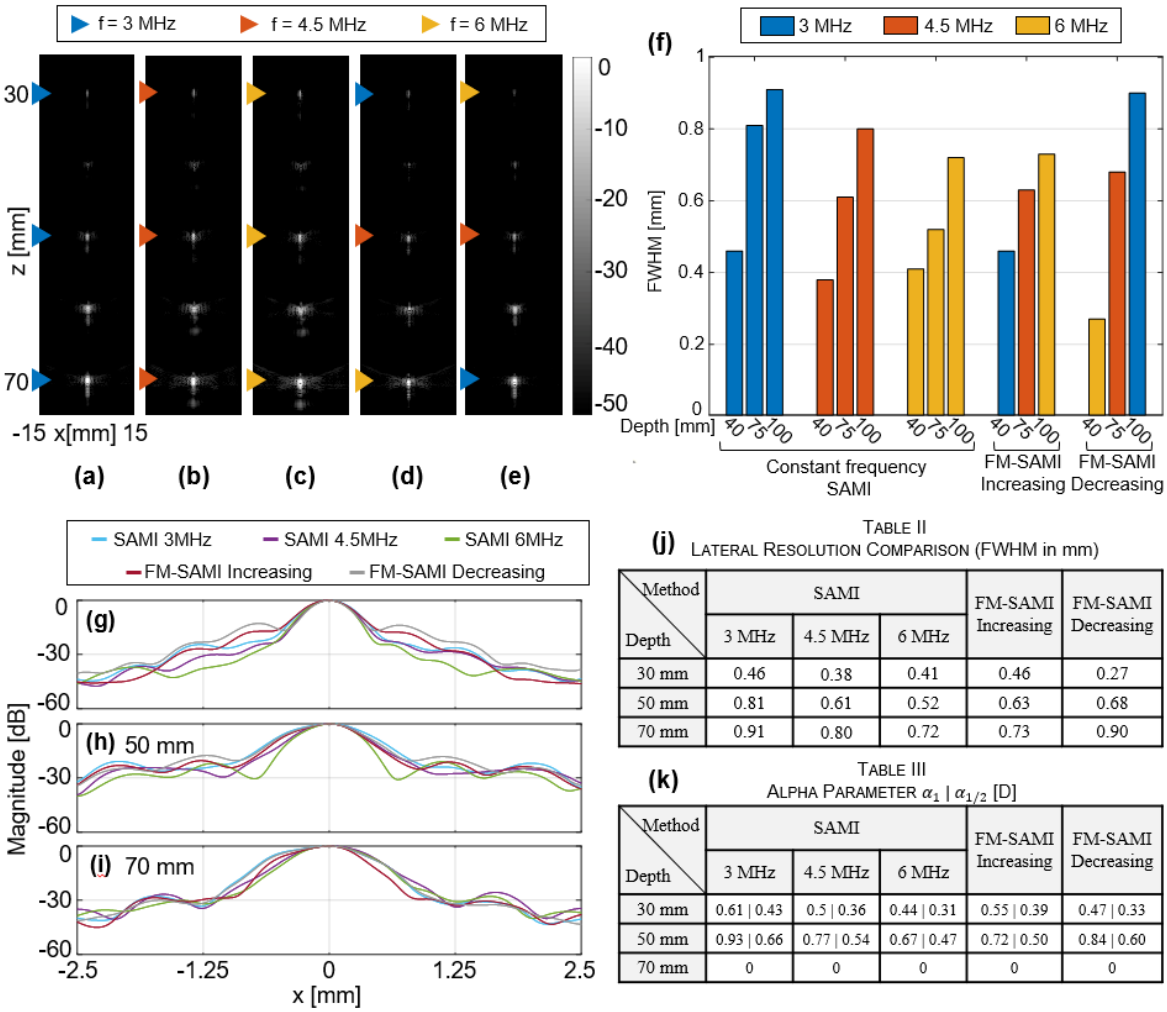

(j) TABLE II
LATERAL RESOLUTION COMPARISON (FWHM in mm)

Method / Depth	SAMI 3 MHz	SAMI 4.5 MHz	SAMI 6 MHz	FM-SAMI Increasing	FM-SAMI Decreasing
30 mm	0.46	0.38	0.41	0.46	0.27
50 mm	0.81	0.61	0.52	0.63	0.68
70 mm	0.91	0.80	0.72	0.73	0.90

(k) TABLE III
ALPHA PARAMETER α_1 | $\alpha_{1/2}$ [D]

Method / Depth	SAMI 3 MHz	SAMI 4.5 MHz	SAMI 6 MHz	FM-SAMI Increasing	FM-SAMI Decreasing
30 mm	0.61 | 0.43	0.5 | 0.36	0.44 | 0.31	0.55 | 0.39	0.47 | 0.33
50 mm	0.93 | 0.66	0.77 | 0.54	0.67 | 0.47	0.72 | 0.50	0.84 | 0.60
70 mm	0	0	0	0	0

Figure 21. Wire target lateral resolution experiments in a water tank. Constant frequency SAMI (a) 3 MHz. (b) 4.5 MHz, and (c) 6 MHz. (d) 'FM-SAMI Increasing' from 3 to 6 MHz. (e) 'FM-SAMI Decreasing' from 6 to 3 MHz. (a)-(e) Focal depth is indicated by triangles and their colors encode the frequencies transmitted. These images are displayed with a 50 dB dynamic range. Axes are common to (a)-(e) and (g)-(i). (f) FWHM for each focal spot in (a)-(e). (g)-(i) Lateral cross sections of the normalized PSFs obtained at the different focal depths (30, 50, 70 mm) in (a)-(e) for each method, respectively. (j) Table II summarizing the FWHM values from (f). (k) Table III summarizing the alpha values for each focus in (j).

Figure 21(g)-(i) presents the lateral cross-section for each focal depth at 30, 50 and 70 mm, as a function of the different SAMI methods. The constant 3 MHz SAMI yielded the widest main

lobe in each of the depths. The main lobe at a depth of 30 mm was the narrowest for the 'FM-SAMI Decreasing' method, and the main lobe at a depth of 70 mm was the narrowest for the 'FM-SAMI Increasing' and 6 MHz constant frequency SAMI methods.

Another consideration is the α parameter. Since the foci locations was fixed for all of the methods, the α parameter varied for each focus in each method. The results are summarized in Table III (Figure 21(k)). Since the focus at 70 mm is created with all of the elements, its α is equal to 0 for all methods. For the other foci the α value changes. The α values do not affect the lateral resolution and the FWHM values.

5.2.3 Contrast experiments

The method's contrast was evaluated by imaging cysts at fixed depths within a commercial tissue-mimicking phantom according to the setup described in 4.2.3. The constant frequency SAMI at 3, 4.5 or 6 MHz, 'FM-SAMI Increasing' and 'FM-SAMI decreasing' methods were compared, but the location of the three axial multifoci were adjusted to the location of the cysts in the phantom (45, 70 and 100 mm) (Figure 22). Once the images were acquired, the contrast of each cyst was calculated based on [43], [45], [46]:

$$\text{Contrast Ratio [dB]} = 20\log_{10}\left(\frac{\mu_i}{\mu_o}\right) \tag{27}$$

where μ_i is the mean value of the pixels within a region inside the object (red squares in Figure 22(a)), and μ_o is the mean value of the pixels within a region in the background outside the object (purple squares in Figure 22(a)). The contrast results for each method are presented in Figure 22(g) and summarized in Table IV. For the deepest focus at 100 mm, the contrast of 'FM-SAMI Decreasing' improved by 7.2 dB compared to 'FM-SAMI Increasing', and was similar to the contrast of constant 3 MHz SAMI. For the shallowest focus at 45 mm, the trend was reversed,

such that the contrast of ‘FM-SAMI Increasing’ improved by 2 dB compared to ‘FM-SAMI Decreasing’, and was similar to the contrast of 6 MHz SAMI.

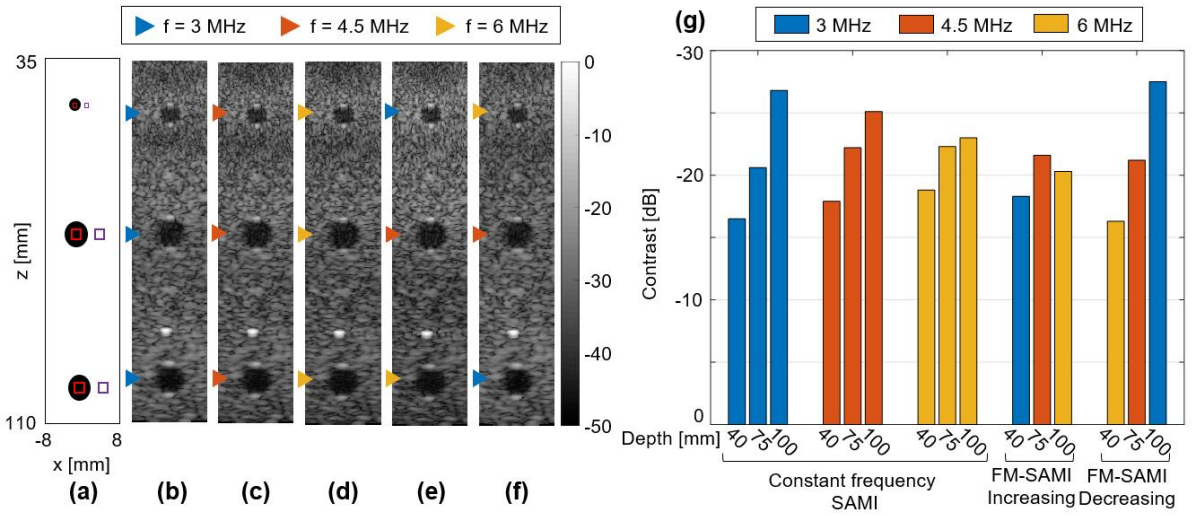

Figure 22. Contrast ratio experiments using cyst targets in a tissue-mimicking phantom. (a) Phantom illustration. The red and purple squares mark the areas inside and outside the cysts used for the contrast ratio calculation. Constant frequency SAMI (a) 3 MHz. (b) 4.5 MHz, and (c) 6 MHz. (e) ‘FM-SAMI Increasing’ from 3 to 6 MHz. (f) ‘FM-SAMI Decreasing’ from 6 to 3 MHz. (b)-(f) Focal depth is indicated by triangles and their colors encode the frequencies transmitted. These images are displayed with a 50 dB dynamic range. Axes are common to (a)-(f). (g) Contrast ratio results for each cyst in (b)-(f). The color encodes the transmitted frequency, with 3 MHz (blue), 4.5 MHz (orange), and 6 MHz (yellow).

TABLE IV
CYST CONTRAST RATIO [dB]

Method / Depth	SAMI 3MHz	SAMI 4.5MHz	SAMI 6MHz	FM-SAMI Increasing	FM-SAMI Decreasing
45 mm	-16.5	-17.9	-18.8	-18.3	-16.3
70 mm	-20.6	-22.2	-22.3	-21.6	-21.2
100 mm	-26.8	-25.1	-23	-20.3	-27.5

Another important parameter is α that varies between each focal spot and each method (Table V). A lo[illegible]dicates that more elements are used for the focus generation, and hence its energy

Method / Depth	SAMI 3MHz	SAMI 4.5MHz	SAMI 6MHz	FM-SAMI Increasing	FM-SAMI Decreasing
45 mm	0.81 | 0.57	0.67 | 0.47	0.58 | 0.41	0.73 | 0.52	0.62 | 0.44
70 mm	>1 | 0.78	0.91 | 0.64	0.79 | 0.56	0.84 | 0.6	0.99 | 0.7
100 mm	0	0	0	0	0

is increased. Thus, the higher the α, the fewer the elements used for its generation. For example, this is why the contrast of the cyst at a depth of 70 mm for constant 3 MHz was the lowest.

TABLE V
ALPHA PARAMETER α_1 | $\alpha_{1/2}$ [D]

Method / Depth	SAMI 3MHz	SAMI 4.5MHz	SAMI 6MHz	FM-SAMI Increasing	FM-SAMI Decreasing
45 mm	0.81 | 0.57	0.67 | 0.47	0.58 | 0.41	0.73 | 0.52	0.62 | 0.44
70 mm	>1 | 0.78	0.91 | 0.64	0.79 | 0.56	0.84 | 0.6	0.99 | 0.7
100 mm	0	0	0	0	0

5.2.4 Ex-vivo experiments

Further validation of the method was performed by imaging a turkey breast (Figure 23). SAMI and FM-SAMI methods with three axial multifoci at 30, 50 and 70 mm were generated and used to image the sample. The foci positions were selected based on features detected in

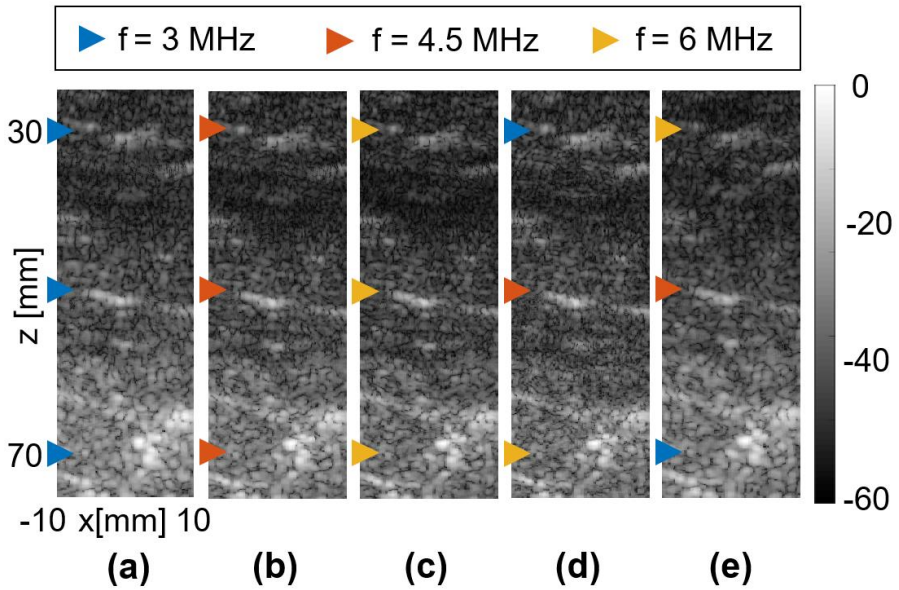

Figure 23. Ex-vivo turkey breast experiments. Constant frequency SAMI (a) 3 MHz. (b) 4.5 MHz, and (c) 6 MHz. (d) 'FM-SAMI Increasing' from 3 to 6 MHz. (e) 'FM-SAMI Decreasing' from 6 to 3 MHz. All subfigures are presented with a 60-dB dynamic range. Axes are common to all subfigures. Focal depth is indicated by triangles and their colors encode the frequencies transmitted.

the ex-vivo sample. Highest resolution was obtained for the 6 MHz frequency, while at the deepest depth of 70 mm, higher contrast was observed for the 3 MHz frequency.

5.2.5 Safety of FM-SAMI

The acoustic safety of the developed methods was evaluated by measuring the mechanical index (MI), the thermal index (TI) and the spatial peak temporal average (Ispta). The MI estimates the likelihood to engender mechanical bioeffects, the TI estimates the likelihood to generate undesired thermal heating bioeffects, and the Ispta represents the overall tissue heating [47].

These parameters were evaluated for the same configuration presented in Figs. 4 and 7, with three foci located at 30, 50, and 70 mm. The transmitted voltage by the Verasonics system was 40 Vpp. The FM-SAMI method's safety parameters were compared to that of constant frequency SAMI at these multiple depths. The needle hydrophone setup, as described in section 4.2.1, was used to evaluate the safety parameters.

The MI was evaluated according to:

$$\mathrm{MI} = \frac{\mathrm{PNP}}{\sqrt{\mathrm{f_c}}} \tag{28}$$

where PNP is the peak negative pressure in MPa and f_c is the center frequency in MHz for each focus [48]. The MI values obtained for each focus, and summarized in Table VI, were below 1.9 [49]. In addition, the MI of each frequency component in the 'FM-SAMI Increasing' and 'FM-SAMI Decreasing' was similar to its corresponding frequency component in the constant frequency SAMI method.

When the ultrasound beam is scanned, as in the case of SAMI, the TI model assumes that the greatest likelihood for the occurrence of undesired thermal effects is near the probe [50], [51].

For soft tissue at surface, the TI was evaluated according to [52]:

$$\mathrm{TIS} = \frac{W_{01} f_c}{210[mW \cdot MHz]} \tag{29}$$

where TIS is the TI for soft tissue, W_{01} is the highest time-averaged acoustic output power value emitted from the most active 1 cm length of the transmitting aperture and the denominator represents the power required to raise the insonated tissue temperature by $1°C$ [53].

The TIS for the different SAMI versions were measured by placing the needle hydrophone 5 mm from the transducer and scanning along 1 cm in lateral direction. This 1 cm was chosen to include the outer part of the aperture, where most of the energy is transmitted in SAMI. The results are summarized in Table VII and remain below the upper limit of 2 [50].

Finally, the Ispta parameter, which provides an estimation of the short-term effects of acoustic transmission on tissue, was calculated as the time average of intensity at a point in space, while the intensity is averaged over a scan repetition period (Table VII). All safety parameters tested were below the safety limit required [49], [50].

TABLE VI
MECHANICAL INDEX

Method / Depth	SAMI 3 MHz		SAMI 4.5 MHz		SAMI 6 MHz		FM-SAMI increasing		FM-SAMI decreasing	
	Pressure [MPa]	Mechanical index	Pressure [MPa]	Mechanical index	Pressure [MPa]	Mechanical index	Pressure [MPa]	Mechanical index	Pressure [MPa]	Mechanical index
30 mm	0.22	0.13	0.21	0.10	0.15	0.06	0.22	0.13	0.17	0.07
50 mm	0.12	0.07	0.21	0.10	0.16	0.06	0.19	0.09	0.22	0.10
70 mm	0.25	0.14	0.22	0.11	0.16	0.07	0.16	0.07	0.24	0.14

Method	SAMI 3 MHz	SAMI 4.5 MHz	SAMI 6 MHz	FM-SAMI increasing	FM-SAMI decreasing	Safety limit
TI	0.0011	0.0015	0.0015	0.0020	0.0022	2

TABLE VII
THERMAL INDEX AND ISPTA

Method	SAMI 3 MHz	SAMI 4.5 MHz	SAMI 6 MHz	FM-SAMI increasing	FM-SAMI decreasing	Safety limit
TI	0.0011	0.0015	0.0015	0.0020	0.0022	2
Ispta [mW/cm2]	0.62	0.55	0.4	0.54	0.64	720

6 Discussion and conclusions

The SAMI method generates simultaneous axial multifoci imaging and enhances the depth of field, but all of the axial multifoci are generated with the same frequency. The FM-SAMI method developed here is an optimized method that makes it possible to transmit each focus at a different frequency simultaneously. This approach is aimed to provide high quality ultrasound imaging over an extended depth of interest and without compromising the framerate, and is useful for applications that require extended depth imaging of high dynamic range targets. Two distinct applications of FM-SAMI were presented here. The first is ‘FM-SAMI Increasing’, where the frequency gradually increases as a function of the foci depths. This approach can achieve a more uniform lateral resolution as a function of depth (i.e. constant FWHM), as is often done in successive focusing [54], [55]. This is not feasible with a constant frequency SAMI that uses the outer parts of the aperture on transmit, so that the aperture size cannot be reduced. Consequently, maintaining a constant F-number and a uniform lateral resolution as a function of depth is not feasible. By increasing the frequency as a function of depth, an effective compensation of the gradually increasing F-number can be achieved. One advantage is the creation of a more uniform image that is preferred by clinicians. Further, it facilitates tissue characterization abilities [56],

enables to accurately segment organs in motion such as in cardiac imaging, conduct nonlinear parameter estimation and improve Doppler velocity estimation [57]. Additionally, depth-independent PSF simplifies the use of image restoration techniques to enhance image quality [13]. Moreover, the method can be useful for applications that utilize nondiffracting beams such as X waves, and Bessel and axicon beams [58]–[60]. These methods maintain uniform DOF at the expense of lateral resolution. 'FM-SAMI Increasing' yields relatively high lateral resolution over an extended DOF, and therefore can be an improved alternative to these methods. Specific clinical applications include transabdominal pelvic ultrasound, where the ultrasound passes through the bladder to reach the female pelvis [61]. The low ultrasound attenuation in the urine, facilitate the transmission of the highest frequency to the deepest depth, which could improve image quality. Similarly, the method can be applied to imaging beyond cysts or fluid-filled areas and provide high quality images of the deep tissues.

In 'FM-SAMI Decreasing', the foci frequency is gradually decreased as a function of depth. This yields a tradeoff between lateral resolution and penetration depth. The shallowest focus' lateral resolution is maximized as a result of the high frequency, while the deepest focus' contrast is enhanced due to reduced attenuation of the beam for the lower frequency. Specific applications of 'FM-SAMI Decreasing' include abdominal imaging of obese patients, where the reduction in frequency as a function of depth improves penetration and image quality [62]–[64]. In addition, it is useful for deep organ imaging [65], [66] such as the gallbladder, liver, and kidneys, and for early diagnosis of abdomen conditions such as abscess, malignancies and cancer [67], [68]. Moreover, the method can be beneficial for diagnosis and monitoring of clinical conditions such as gallstones [69], [70], renal calculi [71], [72], uterine fibroids [73], [74], and myocardial stiffening [75], [76]. Finally, because the frequency reduces with depth, the sensitivity increases

with depth. As a result, less dynamic range compression, such as time gain control, needs to be applied as a function of depth [77].

The real-time FM-SAMI method uses a superposition of wavefronts, each with a different frequency, in a single acoustical transmission. The waveforms are engineered to eliminate the overlap between the superpositioned waveforms. This is done by transmitting the deepest focus with the entire aperture, while the rest of the foci are generated by only using the outer transducer's elements. The fractional aperture that is reduced from the center of the transducer for each focus is denoted by α. On receive, the entire aperture is used. Since the PSF is defined as the product of the transmit and receive apertures, the side lobes and phase patterns are greatly reduced compared to one way focusing [1]. Here, in order to maximize the transmitted energy, apodization was not applied either on transmit or receive. In addition, the pulses used in this paper consisted of single cycles to maximize axial resolution. Moreover, the overlap between superpositioned waveforms increases when increasing the number of transmitted cycles. This translates into a larger α and reduces the energy for the axial multifoci. Thus, to reduce α, single cycle excitation is preferable.

The implementation of FM-SAMI method was carried out using the arbitrary waveform generator feature in an ultrasound programmable system. Each transducer element was programmed to transmit the specific delays that generated each focal spot at a predefined frequency. Since the method does not require post-processing on receive, the built-in beamformer was used and the image was displayed in real time [78]. The transducer used in the experiments was P6-3, with a bandwidth of 3-6 MHz. This was the same transducer used in the constant frequency SAMI paper, and thus facilitate comparison between the methods. The superpositioned waveforms consisted of 3 axial multifoci at frequencies of 3, 4.5 and 6 MHz. An important factor

is the transducer's frequency response, and the fact that it is not uniform across the transducer's bandwidth (Figure 4(k)). Empirically, the frequency responses of all three frequencies used in this study were within 3 dB of the maximal frequency response. When designing the transmitted waveforms, one option is to take the frequency response into account and normalize the waveforms accordingly. However, it would require to intentionally reduce the amplitude of the frequencies that have the best response (in our case, 3 and 4.5 MHz, in order to match that of the 6 MHz). This will reduce the contrast for these frequencies, and not affect their resolution. Here, we chose to maximize the transmitted energy, and therefore transmitted each frequency with its maximal amplitude.

It is likely that this method can be applied to any other commercially available broadband transducer, however, SAMI and FM-SAMI implementation is optimal with phased array transducers. This is because these methods use the entire aperture both on transmit and receive. In phased array transducers, each element's directivity is high and the entire aperture can contribute to the generation of the focal spot. On the other hand, linear arrays often utilize subapertures to create the focal spot. Each subaperture is composed of a few (typically 5-20) adjacent elements. The small number of elements used for the generation of each focal spot makes the implementation of the SAMI methods more limited. In addition, linear arrays usually have higher frequencies and designed for shallower imaging. This makes focusing with the entire aperture even more challenging. Phased array transducers typically have lower center frequencies designed to image large sectors where increased DOF is required. As a result, they are composed of smaller elements (on the order of half the wavelength), that contribute to their higher directivity. Since the transducer's number of elements is similar between phased, linear and curved arrays, D is often smaller for phased arrays compared to linear arrays that have larger

elements. These considerations should be taken into account when implementing the SAMI method.

The standard SAMI method was previously compared to synthetic aperture imaging, two-way focusing using a single focus at various depths, and to successive focusing [1]. Here, our aim was to validate the FM-SAMI methods, 'FM-SAMI Decreasing' and 'FM-SAMI Increasing', and compare them to the standard constant frequency SAMI, that was considered as the baseline. When comparing the FM-SAMI method to single frequency SAMI, foci with the same frequency for each method yielded similar lateral resolution and contrast. If variations in contrast were detected, these can be attributed to the fact that the α values can change across methods, since α is frequency dependent. The numerical simulations were focused on lateral resolution, beam width, DOF and attenuation. Simulations indicate a tradeoff between lateral resolution, DOF and attenuation as a function of frequency. Lower frequencies yield larger DOF and lower attenuation at the expense of a reduced lateral resolution. Thus, by implementing 'FM-SAMI Decreasing', a more continuous depth of field alongside a more uniform attenuation as a function of axial depth can be obtained. 'FM-SAMI Increasing' yielded the highest uniformity of lateral resolution, by reducing the FWHM of the deepest and intermediate foci, compared to constant frequency SAMI. However, since the deepest focus is generated with the highest frequency of 6 MHz, the attenuation increased and therefore the contrast is reduced compared to transmitting all foci at a constant frequency of 3 MHz. In a practical implementation, attenuation is further affected by the transducer's frequency response. For the P6-3, the 6 MHz frequency response is reduced by 35% compared to 3 MHz. Therefore, the attenuation for the highest frequency is further degraded compared to the values predicted. For 'FM-SAMI Decreasing', the lateral resolution of the shallowest focus generated at 6 MHz was maximized, while the contrast of the deepest focus

generated at 3 MHz was enhanced by 4.5 dB compared to the constant frequency SAMI at 6 MHz. The SAMI methods can be engineered to any depth larger than D (given that focusing can be done with the entire aperture). Here, standard depths up to 100 mm were chosen in order to demonstrate the methods performance. In terms of acoustic safety, for the standard parameters used here, the SAMI and FM-SAMI methods comply with the acoustic safety regulations.

One of the limitations of this study stems from its practical implementation using a programmable ultrasound system. On receive, the beamformer uses a predefined constant center frequency. Therefore, although different frequencies were used in the superpositioned waveform on transmit, the frequency for the receive beamforming was set to 4.5 MHz. Since the two-way PSF is the product of the transmit and receive PSFs, the maximal improvement in lateral resolution did not reach the theoretical values (except for the case of transmitting a center frequency of 4.5 MHz). In order to achieve the theoretical values, frequency-dependent beamforming should be applied to each focus. However, since the comparison between the methods was carried out experimentally, and all methods used the same constant receive frequency, the comparison is valid. Future implementation could further improve the method by adding a time sliding filter [18]–[20], or demodulation with a sliding CW frequency [79], [80], on receive. Such approaches will enable to tune the frequency for each beamformed focus. Another future application includes a frequency-dependent steering angle, that could be used for grating lobes elimination [81]. The method could also be combined with techniques for PSF engineering in order to reduce side lobes [43].

Overall, this improved frequency-dependent FM-SAMI method yields high quality imaging at an extended field of interest. The method can optimize tradeoffs between lateral resolution and

penetration depth. Validation of the method was performed through numerical simulations and experiments on resolution and contrast targets.

7 References

[1] A. Ilovitsh, T. Ilovitsh, J. Foiret, D. N. Stephens, and K. W. Ferrara, "Simultaneous Axial Multifocal Imaging Using a Single Acoustical Transmission: A Practical Implementation," *IEEE Trans. Ultrason. Ferroelectr. Freq. Control*, vol. 66, no. 2, pp. 273–284, 2019, doi: 10.1109/TUFFC.2018.2885080.

[2] R. M. Nally, "Ultrasound Imaging," *Handb. Vis. Disp. Technol.* Berlin, Gerrmany: Springer, 2012, pp. 373–383, 2012, doi: 10.1007/978-3-540-79567-4_30.

[3] O. H. Baltarowich *et al.*, "National ultrasound curriculum for medical students," *Ultrasound Q.*, vol. 30, no. 1, pp. 13–19, 2014, doi: 10.1097/RUQ.0000000000000066.

[4] K. K. Shung, "Diagnostic Ultrasound: Past, Present, and Future," *J. Med. Biol. Eng.*, vol. 31, no. 6, pp. 371–374, doi: 10.5405/jmbe.871.

[5] Thomas L. Szabo, *Diagnostic Ultrasound Imaging: Inside Out*, 1st ed. Elsevier Science & Technology, 2004.

[6] J. Vogel, N. Bom, J. Ridder, and C. Lancee, "Transducer design considerations in dynamic focusing," *Ultrasound Med. Biol.*, vol. 5, no. 2, pp. 187–193, Jan. 1979, doi: 10.1016/0301-5629(79)90087-5.

[7] K. Thomenius, "Evolution of ultrasound beamformers. 1996 IEEE," *Ultrason. Symp. Proc.*, vol. 2, pp. 1615–1622, 1996.

[8] T. Ilovitsh, A. Ilovitsh, J. Foiret, B. Z. Fite, and K. W. Ferrara, "Acoustical structured illumination for super-resolution ultrasound imaging," *Commun. Biol.*, vol. 1, no. 1, p. 3,

Jan. 2018, doi: 10.1038/s42003-017-0003-5.

[9] G. Matrone, A. S. Savoia, G. Caliano, and G. Magenes, “Depth-of-field enhancement in Filtered-Delay Multiply and Sum beamformed images using Synthetic Aperture Focusing,” *Ultrasonics*, vol. 75, pp. 216–225, Mar. 2017, doi: 10.1016/j.ultras.2016.11.022.

[10] J. A. Jensen, S. I. Nikolov, K. L. Gammelmark, and M. H. Pedersen, “Synthetic aperture ultrasound imaging,” *Ultrasonics*, vol. 44, no. SUPPL., pp. e5–e15, Dec. 2006, doi: 10.1016/J.ULTRAS.2006.07.017.

[11] S. H. Contreras Ortiz, T. Chiu, and M. D. Fox, “Ultrasound image enhancement: A review,” *Biomed. Signal Process. Control*, vol. 7, pp. 419–428, 2012, doi: 10.1016/j.bspc.2012.02.002.

[12] S. M. Maslak, “Computed sonography,” *Ultrasound Annu. vol. 8(3)*, pp. 1–16, 1985.

[13] J. Y. Lu, H. Zou, and J. F. Greenleaf, “Biomedical ultrasound beam forming,” *Ultrasound Med. Biol.*, vol. 20, no. 5, pp. 403–428, Jan. 1994, doi: 10.1016/0301-5629(94)90097-3.

[14] Verasonics, Kirkland, WA, USA. Accessed: Jun. 1, 2018. [Online]. Available: http://verasonics.com

[15] J. Flynn, R. Daigle, L. Pflugrath, K. Linkhart, and P. Kaczkowski, “Estimation and display for vector Doppler imaging using planewave transmissions,” *IEEE Int. Ultrason. Symp. IUS*, pp. 413–418, 2011, doi: 10.1109/ULTSYM.2011.0099.

[16] J. A. Hossack *et al.*, “Ultrasound imaging system and method for improving resolution and operation,” 5 873 830, Aug. 22, 1997.

[17] C. R. Cole and A. Gee, “Method and apparatus for transmit beamformer system,” 5 856 955, Jul. 10, 1997.

[18] J. A. Hossack, “Extended focal depth imaging for medical ultrasound,” in *1996 IEEE Ultrasonics Symposium. Proceedings*, vol. 2, pp. 1535–1540, doi: 10.1109/ULTSYM.1996.584375.

[19] S. Zhou and J. A. Hossack, “Dynamic-transmit focusing using time-dependent focal zone and center frequency,” *IEEE Trans. Ultrason. Ferroelectr. Freq. Control*, vol. 50, no. 2, pp. 142–152, 2003, doi: 10.1109/TUFFC.2003.1182118.

[20] J. A. Hossack, J. W. Alisson, A. Gee, and M. O’Donnell, “Ultrasonic Doppler imaging system with frequency dependent focus,” 5 891 037, Dec. 18, 1997.

[21] L. Demi, M. D. Verweij, and K. W. A. Van Dongen, “Parallel transmit beamforming using orthogonal frequency division multiplexing applied to harmonic Imaging-A feasibility study,” *IEEE Trans. Ultrason. Ferroelectr. Freq. Control*, vol. 59, no. 11, pp. 2439–2447, Nov. 2012, doi: 10.1109/TUFFC.2012.2476.

[22] L. Demi, A. Ramalli, G. Giannini, and M. Mischi, “In Vitro and in Vivo tissue harmonic images obtained with parallel transmit beamforming by means of orthogonal frequency division multiplexing,” *IEEE Ultrason. Symp. Proc.*, vol. 62, no. March 2016, pp. 230–5, 2015, doi: 10.1109/TUFFC.2014.006599.

[23] R. J. Pittaro and S. Carlos, “Ultrasound system with dynamic transmit focus,” 5 113 706, Jul. 03, 1990.

[24] Thomas L. Szabo, *Diagnostic Ultrasound Imaging: Inside Out*, 2nd ed. Elsevier Science & Technology, 2013.

[25] H. Azhari, *Basics of biomedical ultrasound for engineers*. John Wiley & Sons, 2010.

[26] T. Szasz, “Advanced beamforming techniques in ultrasound imaging and the associated inverse problems,” Universit´e Toulouse 3 Paul Sabatier (UT3 Paul Sabatier).

[27] A. Anvari, F. Forsberg, and A. E. Samir, “A primer on the physical principles of tissue harmonic imaging,” *Radiographics*, vol. 35, no. 7, pp. 1955–1964, 2015, doi: 10.1148/rg.2015140338.

[28] J. Prince and J. Links, "Medical imaging: signals and systems". *Prentice Hall*, 2nd edition, 2006.

[29] H. Azhari, J. A. Kennedy, N. Weiss, and L. Volokh, “Ultrasound Imaging,” Phys. Med. Biol., vol. 51. no. 13, pp. 321–364, 2020, doi: 10.1007/978-3-030-35326-1_7.

[30] Q. Zhou, K. H. Lam, H. Zheng, W. Qiu, and K. K. Shung, “Piezoelectric single crystal ultrasonic transducers for biomedical applications,” *Progress in Materials Science*, vol. 66. pp. 87–111, 2014, doi: 10.1016/j.pmatsci.2014.06.001.

[31] R. Panda, *Development of novel piezoelectric composites by solid freeform fabrication techniques*. ProQuest Dissertations and Theses, 1998.

[32] J. A. Jensen, “Linear description of ultrasound imaging systems: Notes for the International Summer School on Advanced Ultrasound Imaging,” Technical University of Denmark, Department of Electrical Engineering, 1999.

[33] Y. Li *et al.*, “Difference-Frequency Ultrasound Imaging with Non-Linear Contrast,” *IEEE Trans. Med. Imaging*, vol. 39, no. 5, pp. 1759–1766, 2020, doi: 10.1109/TMI.2019.2957280.

[34] J. M. Mari and C. Cachard, “Acquire real-time RF digital ultrasound data from a commercial scanner”, *Technical Acoustics*, vol. 3, no. January 2007, pp. 28-43, 2007.

[35] E. D. Light, V. Lieu, and S. W. Smith, “Progress in ring array transducers for real-time 3D ultrasound guidance of cardiac interventional devices,” *Ultrason. Imaging*, vol. 33, no. 3, pp. 197–204, 2011.

[36] J. Powers and F. Kremkau, “Medical ultrasound systems”, *Interface focus*, vol. 1, no. 4, pp. 477-489, doi: 10.1098/rsfs.2011.0027.

[37] K. Ranganathan and W. F. Walker, “A novel beamformer design method for medical ultrasound. Part I: Theory,” *IEEE Trans. Ultrason. Ferroelectr. Freq. Control*, vol. 50, no. 1, pp. 15–24, 2003, doi: 10.1109/TUFFC.2003.1176522.

[38] E. Alasaarela and J. Koivukangas, “Evaluation of image quality of ultrasound scanners in medical diagnostics,” *J. Ultrasound Med.*, vol. 9, no. 1, pp. 23–34, Jan. 1990, doi: 10.7863/jum.1990.9.1.23.

[39] J.-L. Robert, R. Erkamp, S. Korukonda, F. Vignon, and E. Radulescu, “Using redundancy of round-trip ultrasound signal for non-continuous arrays: Application to gap and blockage compensation,” *J. Acoust. Soc. Am.*, vol. 138, no. 5, pp. 3375–3382, 2015, doi: 10.1121/1.4934952.

[40] T. Ilovitsh, A. Ilovitsh, J. Foiret, and K. W. Ferrara, “Imaging beyond ultrasonically-impenetrable objects,” *Sci. Rep.*, vol. 8, no. 1, p. 5759, Dec. 2018, doi: 10.1038/s41598-018-23776-7.

[41] G. S. Kino, *Acoustic Waves: Devices, Imaging, and Analog Signal Processing*. Englewood Cliffs, NJ, USA: Prentice-Hall, 1987.

[42] W. D. O’Brien, “Ultrasound-biophysics mechanisms,” *Prog. Biophys. Mol. Biol.*, vol. 93, no. 1–3, pp. 212–255, Jan. 2007, doi: 10.1016/J.PBIOMOLBIO.2006.07.010.

[43] A. Ilovitsh, T. Ilovitsh, and K. W. Ferrara, “Multiplexed ultrasound beam summation for side lobe reduction,” *Sci. Rep.*, vol. 9, no. 1, pp. 3–10, 2019, doi: 10.1038/s41598-019-50317-7.

[44] M. O. Culjat, D. Goldenberg, P. Tewari, and R. S. Singh, “A Review of Tissue Substitutes

for Ultrasound Imaging," *Ultrasound Med. Biol.*, vol. 36, no. 6, pp. 861–873, Jun. 2010, doi: 10.1016/j.ultrasmedbio.2010.02.012.

[45] Y. Deng, M. L. Palmeri, N. C. Rouze, G. E. Trahey, C. M. Haystead, and K. R. Nightingale, "Quantifying Image Quality Improvement Using Elevated Acoustic Output in B-Mode Harmonic Imaging," *Ultrasound Med. Biol.*, vol. 43, no. 10, pp. 2416–2425, Oct. 2017, doi: 10.1016/j.ultrasmedbio.2017.06.024.

[46] M. Bismuth, S. Katz, H. Rosenblatt, M. Twito, R. Aronovich, and T. Ilovitsh, "Acoustically Detonated Microbubbles Coupled with Low Frequency Insonation: Multiparameter Evaluation of Low Energy Mechanical Ablation," *Bioconjug. Chem.*, vol. 33, no. 6, pp. 1069–1079, Jun. 2022, doi: 10.1021/acs.bioconjchem.1c00203.

[47] "Marketing Clearance of Diagnostic Ultrasound Systems and Transducers", Ultrasound, FDA (Food and Drug Administration), Maryland USA, 2019. [Online]. Available: https://www.regulations.gov.

[48] T. Ilovitsh *et al.*, "Enhanced microbubble contrast agent oscillation following 250 kHz insonation," *Sci. Rep.*, vol. 8, no. 1, pp. 1–15, Dec. 2018, doi: 10.1038/s41598-018-34494-5.

[49] T. R. Nelson, J. B. Fowlkes, J. S. Abramowicz and C. C. Church, "Ultrasound biosafety considerations for the practicing sonographer and sonologist", J. Ultrasound Med., vol. 28, no. 2, pp. 139-150, 2009. [online] Available: https://onlinelibrary.wiley.com/doi/abs/10.7863/jum.2009.28.2.139.

[50] W. D. O'Brien *et al.*, "The Risk of Exposure to Diagnostic Ultrasound in Postnatal Subjects," *J. Ultrasound Med.*, vol. 27, no. 4, pp. 517–535, Apr. 2008, doi: 10.7863/jum.2008.27.4.517.

[51] M. G. Curley, “Soft tissue temperature rise caused by scanned, diagnostic ultrasound,” *IEEE Trans. Ultrason. Ferroelectr. Freq. Control*, vol. 40, no. 1, pp. 59–66, Jan. 1993, doi: 10.1109/58.184999.

[52] T. A. Bigelow *et al.*, “The Thermal Index,” *J. Ultrasound Med.*, vol. 30, no. 5, pp. 714–734, 2011, doi: 10.7863/jum.2011.30.5.714.

[53] J. G. Abbott, “Rationale and derivation of MI and TI—a review,” *Ultrasound Med. Biol.*, vol. 25, no. 3, pp. 431–441, Mar. 1999, doi: 10.1016/S0301-5629(98)00172-0.

[54] B. Robinson and C. Cooley, “Synthetic dynamic transmit focus,” *Proc. IEEE Ultrason. Symp.*, vol. 2, no. i, pp. 1209–1214, 2000, doi: 10.1109/ULTSYM.2000.921540.

[55] R. J. Zemp, C. K. Abbey, and M. F. Insana, “Linear System Models for Ultrasonic Imaging: Application to Signal Statistics,” *IEEE Trans. Ultrason. Ferroelectr. Freq. Control*, vol. 50, no. 6, pp. 642–654, 2003.

[56] J. T. Ylitalo and H. Ermert, “Ultrasound Synthetic Aperture Imaging: Monostatic Approach,” *IEEE Trans. Ultrason. Ferroelectr. Freq. Control*, vol. 41, no. 3, pp. 333–339, 1994, doi: 10.1109/58.285467.

[57] M. K. Jeong, T. K. Song, and S. B. Park, “Generation of sine wave by a one-dimensional array for applications in ultrasonic imaging,” *IEEE Trans. Ultrason. Ferroelectr. Freq. Control*, vol. 43, no. 2, pp. 285–295, 1996, doi: 10.1109/58.485955.

[58] C. B. Burckhardt, H. Hoffmann, and P. A. Grandchamp, “Ultrasound Axicon: a device for focusing over a large depth,” *J. Acoust. Soc. Am.*, vol. 54, no. 6, pp. 1628–1630, Dec. 1973, doi: 10.1121/1.1914459.

[59] D. K. Hsu, F. J. Margetan, and D. O. Thompson, “Bessel beam ultrasonic transducer: Fabrication method and experimental results,” *Appl. Phys. Lett.*, vol. 55, no. 20, pp. 2066–

2068, 1989, doi: 10.1063/1.102107.

[60] J. Y. Lu and J. F. Greenleaf, “Experimental Verification of Nondiffracting X Waves,” *IEEE Trans. Ultrason. Ferroelectr. Freq. Control*, vol. 39, no. 3, pp. 441–446, 1992, doi: 10.1109/58.143178.

[61] D. Fischerova, “Ultrasound scanning of the pelvis and abdomen for staging of gynecological tumors: A review,” *Ultrasound Obstet. Gynecol.*, vol. 38, no. 3, pp. 246–266, Sep. 2011, doi: 10.1002/UOG.10054.

[62] C. Caraiani, Y. Dong, A. G. Rudd, and C. F. Dietrich, “Reasons for inadequate or incomplete imaging techniques,” *Med. Ultrason.*, vol. 20, no. 4, pp. 498–507, Dec. 2018, doi: 10.11152/MU-1736.

[63] P. Glanc, B. E. O’Hayon, D. K. Singh, S. A. J. Bokhari, and C. V. Maxwell, “Challenges of pelvic imaging in obese women,” *Radiographics*, vol. 32, no. 6, pp. 1839–1862, Oct. 2012, doi: 10.1148/RG.326125510/ASSET/IMAGES/LARGE/125510FIG12.JPEG.

[64] R. N. Uppot, D. V. Sahani, P. F. Hahn, M. K. Kalra, S. S. Saini, and P. R. Mueller, “Effect of obesity on image quality: Fifteen-year longitudinal study for evaluation of dictated radiology reports,” *Radiology*, vol. 240, no. 2, pp. 435–439, Aug. 2006, doi: 10.1148/RADIOL.2402051110/ASSET/IMAGES/LARGE/F06AU19L02X.JPEG.

[65] H. Tai, M. Khairalseed, and K. Hoyt, “Adaptive attenuation correction during H-scan ultrasound imaging using K-means clustering,” *Ultrasonics*, vol. 102, p. 105987, Mar. 2020, doi: 10.1016/J.ULTRAS.2019.105987.

[66] E. Tiran *et al.*, “Multiplane wave imaging increases signal-to-noise ratio in ultrafast ultrasound imaging,” *Phys. Med. Biol.*, vol. 60, no. 21, p. 8549, Oct. 2015, doi: 10.1088/0031-9155/60/21/8549.

[67] S. Kavia and G. Rottenberg, “Ultrasound in surgery,” *Surg.*, vol. 23, no. 5, pp. 165–167, May 2005, doi: 10.1383/SURG.23.5.165.65499.

[68] C. L. Morgan, W. S. Trought, O. T. von Ramm, and F. L. Thurstone, “Abdominal and obstetric applications of a dynamically focused phased array real time ultrasound system,” *Clin. Radiol.*, vol. 31, no. 3, pp. 277–286, 1980, doi: 10.1016/S0009-9260(80)80217-0.

[69] D. Gandhi *et al.*, “A pictorial review of gall stones and its associated complications,” *Clin. Imaging*, vol. 60, no. 2, pp. 228–236, Apr. 2020, doi: 10.1016/J.CLINIMAG.2019.11.015.

[70] T. Neitlich and J. Neitlich, “The imaging evaluation of cholelithiasis in the obese patient-ultrasound vs CT cholecystography: Our experience with the bariatric surgery population,” *Obes. Surg.*, vol. 19, no. 2, pp. 207–210, Feb. 2009, doi: 10.1007/S11695-008-9582-Z/FIGURES/3.

[71] S. Eskandari, S. Meshgini, and A. Farzamnia, “Using a Novel Algorithm in Ultrasound Images to Detect Renal Stones,” *Lect. Notes Electr. Eng.*, vol. 770, pp. 755–767, 2022, doi: 10.1007/978-981-16-2406-3_58/FIGURES/5.

[72] S. Selvarani and P. Rajendran, “Detection of Renal Calculi in Ultrasound Image Using Meta-Heuristic Support Vector Machine,” *J. Med. Syst.*, vol. 43, no. 9, pp. 1–9, Sep. 2019, doi: 10.1007/S10916-019-1407-1/TABLES/2.

[73] B. Stoelinga *et al.*, “Contrast-Enhanced Ultrasound Imaging of Uterine Disorders: A Systematic Review,” *Ultrason. Imaging*, vol. 43, no. 5, pp. 239–252, Sep. 2021, doi: 10.1177/01617346211017462.

[74] S. Peng *et al.*, “Intraprocedure contrast enhanced ultrasound: The value in assessing the effect of ultrasound-guided high intensity focused ultrasound ablation for uterine fibroids,” *Ultrasonics*, vol. 58, pp. 123–128, Apr. 2015, doi:

10.1016/J.ULTRAS.2015.01.005.

[75] M. Couade *et al.*, “In Vivo quantitative mapping of myocardial stiffening and transmural anisotropy during the cardiac cycle,” *IEEE Trans. Med. Imaging*, vol. 30, no. 2, pp. 295–305, 2011, doi: 10.1109/TMI.2010.2076829.

[76] S. J. Hsu, R. R. Bouchard, D. M. Dumont, P. D. Wolf, and G. E. Trahey, “In Vivo Assessment of Myocardial Stiffness with Acoustic Radiation Force Impulse Imaging,” *Ultrasound Med. Biol.*, vol. 33, no. 11, pp. 1706–1719, Nov. 2007, doi: 10.1016/J.ULTRASMEDBIO.2007.05.009.

[77] R. A. Harris, D. H. Follett, M. Halliwell, and P. N. T. Wells, “Ultimate limits in ultrasonic imaging resolution,” *Ultrasound Med. Biol.*, vol. 17, no. 6, pp. 547–558, 1991, doi: 10.1016/0301-5629(91)90025-R.

[78] K. T. Karlinsky and T. Ilovitsh, “Ultrasound Frequency Mixing for Enhanced Contrast Harmonic Imaging of Microbubbles,” *IEEE Trans. Ultrason., Ferroelectr., Freq. Control*, vol. 69, no. 8, pp. 2414–2424, Aug. 2022, doi: 10.1109/TUFFC.2022.3179471.

[79] P. Wang, Y. Shen, and Q. Wang, “Gaussian wavelet based dynamic filtering (GWDF) method for medical ultrasound systems,” *Ultrasonics*, vol. 46, no. 2, pp. 168–176, May 2007, doi: 10.1016/J.ULTRAS.2007.01.005.

[80] H. Yoon, K. Jeon, H. Lee, K. Kim, and C. Yoon, “Effective Adaptive Dynamic Quadrature Demodulation in Medical Ultrasound Imaging,” *J Electr Eng Technol*, vol. 13, no. 1, pp. 468–475, 2018, doi: 10.5370/JEET.2018.13.1.468.

[81] C. T. Lancée, R. Daigle, D. J. Sahn, and J. M. Thijssen, “Transducer applications in echocardiology,” *Ultrasonics*, vol. 23, no. 5, pp. 199–205, 1985, doi: 10.1016/0041-624X(85)90014-9.

תקציר

אולטרסאונד הינה אחת משיטות ההדמיה הנפוצות ביותר כיום לאבחון רפואי. פרט לכך שמדובר בשיטת הדמיה המאפשרת הדמיה בזמן אמת ובעלות נמוכה, שיטה זו נחשבת גם לשיטת הדמיה בטוחה שכן היא אינה כוללת שימוש בקרינה מייננת. בנוסף, היא בעלת עומק חדירה גדול וכן אינה פולשנית. שיטת הדימות הנפוצה והאיכותית ביותר משתמשת בפיקוס הלוך-חזור. בשיטה זו, חזית הגל האקוסטית מפוקסת לנקודת מוקד הן בשלב השידור והן בשלב החזור למתמר. שיטת דימות זו מניבה רזולוציה לטרלית גבוהה, מגבירה את יחס האות לרעש ומאפשרת עומק חדירה גדול יותר בהשוואה לשיטות ההדמיה האולטראסוניות האחרות.

אחת המגבלות העיקריות הכרוכות בשימוש בפיקוס הלוך-חזור נובעת מהעובדה שבשלב השידור ניתן למקד את הסיגנל הנשלח רק לעומק בודד. לכן, בפועל, היתרונות של השיטה מוגבלים מבחינה מרחבית רק לאזור הפוקוס. האזור האקסיאלי שבו הכתם מפוקס נקרא גם עומק המוקד. כדי לשדר מספר נקודות פוקוס לעומקים שונים ולהגדיל את עומק המוקד ואת אזור העניין בתמונה, מקובל להשתמש בשיטה דינמית לעדכון הפוקוס. בשיטה זו, מספר תמונות נרכשות תוך עדכון מיקום הפוקוס לאורך הציר האקסיאלי בכל רכישה. כיום, זו השיטה הממומשת כמעט בכל מערכת אולטרסאונד קלינית, אשר מספקת תמונה מפוקסת ובאיכות גבוהה לאורך טווחי עומק גדולים יותר. חסרון השיטה טמון בקצב הרכישה שמואט בצורה פרופורציונלית למספר הפוקוסים שנוצרים.

לאחרונה, פותחה שיטת הדמיה מולטיפוקלית (SAMI) המבוססת על סופרפוזיציה של חזיתות הגל הנשלחות. כל חזית גל מפוקסת לעומק שונה ושידורם יחד בו זמנית מאפשר לייצר מספר פוקוסים בעומקים שונים במקביל. בצורה זו, ניתן לשפר את איכות התמונה מבלי לפגוע בקצב הרכישה. עם זאת, כיוון שכל הפוקוסים הנשלחים משודרים בתדר מרכזי קבוע, השיטה דורשת להתפשר בין בחירת תדר גבוה שיאפשר רזולוציה לטרלית גבוהה מצד אחד, לבין בחירת תדר נמוך שיאפשר להגביר את עומק החדירה של חזיתות שכן תדרים גבוהים מונחתים בצורה משמעותית יותר כפונקציה של עומק ההדמיה.

במחקר הזה פיתחנו אפשרות לריבוב תדר עבור כל אחד מהפוקוסים שנוצרים בשיטה של SAMI. במקרה הזה, כל חזית גל מיוצרת בתדירות אחרת. לאחר מכן, מתבצעת סופרפוזיציה של חזיתות הגל השונות אשר שידורן ע"י המתמר מתבצע בשליחה בודדת. ישנן שתי אפשרויות עיקריות לאופן ריבוב התדרים בשידור; על ידי הגדלת התדר באופן

הדרגתי כפונקציה של עומק הפוקוס, ניתן לפצות על הרזולוציה הלטרלית שיורדת כפונקציה של העומק וכך להשיג רזולוציה לטרלית אחידה יותר לאורך כל עומק הסריקה. לחילופין, על ידי הקטנה הדרגתית של תדרי השידור כפונקציה של עומק הפוקוס, מתקבלים עומק חדירה וניגודיות משופרים.

שיטה זו, המכונה SAMI מרובה תדרים (FM-SAMI), מתוארת בצורה אנליטית ומאומתת באמצעות ניסויי רזולוציה וניגודיות אשר בוצעו על מטרות רזולוציה, על פנטום מדמה רקמה וכן על דגימות ביולוגיות ex-vivo. זהו היישום הראשון של הדמיה מולטיפוקלית ליצירת מספר נקודות פוקוס בשליחה בודדת בשילוב ריבוב תדרים. השיטה מאפשרת הדמיה בזמן אמת, באיכות גבוהה, בעומק מוקד גבוה ובקצב הדמיה מהיר.

אוניברסיטת תל אביב

הפקולטה להנדסה ע"ש איבי ואלדר פליישמן

בית הספר לתארים מתקדמים ע"ש זנדמן-סליינר

פיתוח שיטת הדמיה מולטיפוקלית באמצעות ריבוב תדרים תלוי עומק

חיבור זה הוגש כעבודת גמר לקראת התואר "מוסמך אוניברסיטה" בהנדסה ביו-רפואית

על-ידי

אביטבול רפאל

העבודה נעשתה במחלקה להנדסה ביו-רפואית

בהנחיית ד"ר טלי אילוביץ

אוניברסיטת תל אביב

הפקולטה להנדסה ע"ש איבי ואלדר פליישמן

בית הספר לתארים מתקדמים ע"ש זנדמן-סליינר

פיתוח שיטת הדמיה מולטיפוקלית באמצעות ריבוב תדרים תלוי עומק

חיבור זה הוגש כעבודת גמר לקראת התואר "מוסמך אוניברסיטה" בהנדסה ביו-רפואית

על-ידי

אביטבול רפאל

העבודה נעשתה במחלקה להנדסה ביו-רפואית

בהנחיית ד"ר טלי אילוביץ